Waves in Magnetic Structures in Solar Atmosphere

A thesis submitted towards partial fulfilment of
BS-MS Dual Degree Programme

by
Ajay Kumar Tiwari
Reg. No. 20111009

under the guidance of

Prof. Dipankar Banerjee
Indian Institute of Astrophysics, Bangalore

Indian Institute of Science Education and Research
Pune
November 17, 2016

Certificate

This is to certify that this thesis entitled Waves in Magnetic Structures in Solar Atmosphere submitted towards the partial fulfilment of the BS-MS dual degree programme at the Indian Institute of Science Education and Research Pune represents original research carried out by Ajay Kumar Tiwari at the Indian Institute of Astrophysics, Bangalore, under the supervision of Prof. Dipankar Banerjee during the academic year 2016.

Student	Supervisor
Ajay Kumar	Dr. Dipankar
Tiwari	Banerjee

Declaration

I hereby declare that the matter embodied in the report entitled Waves in Magnetic Structures in Solar Atmosphere are the results of the investigations carried out by me at the Indian Institute of Astrophysics, Bangalore under the supervision of Prof. Dipankar Banerjee and the same has not been submitted elsewhere for any other degree.

Student	Supervisor
AJAY KUMAR TIWARI	PROF. DIPANKAR BANERJEE

Summary

We studied the properties of Sun. The energy generation and transport mechanisms as well as the generation of magnetic field which ultimately lead to teh formation of different types of structures in the atmosphere of Sun. Further we studied the wave properties of several magnetic field structures in solar atmosphere, such as plumes, coronal loops and prominences. These waves are important proxy for the surrounding medium of these magnetic structures. In this report we focus on the wave properties in an open magnetic field structure, such as plume. Waves in an on-disk plume observed by Atmospheric Imaging Assembly (AIA) onboard Solar Dynamic Observatory (SDO). An X1.0-class flare from the NOAA active region AR 12017 was recorded in GOES at 17:35 UT on 29 March 2014. A shock wave was generated after the flare which interacts with plume. The incoming shock hits and compresses the plasma inside the plume, thereby triggering the oscillations. We also observed the signature of reflection in the plume. The estimated speed of the shock is comparable to the local acoustic speed. We conclude that the these oscillations are standing oscillations. The time period of these waves is found to be roughly 11 mins and the velocity was found to be 108 km/sec. To further understand the nature of density profile required to support such an oscillation we performed the differential emmission measure (DEM) analysi s on the AIA image sequence, which gives us the density profile in the plume that supports the standing oscillation in the open loop. This is a first identification of such standing mode oscillations in open magnetic field structures in the solar atmosphere.

For my parents.

Acknowledgements

First and foremost, I would like to express my sincere gratitude to my advisor Prof. Dipanakar Banerjee for the continuous support of my Masters' thesis, for his patience, motivation, enthusiasm and encouragement. His guidance has helped me in research and writing of this thesis. Besides my advisor, I would like to thank my co-advisor Dr. Parsad Subramanian, for his encouragement, insightful comments, and hard questions. My sincere thanks also goes to Vaibhav Pant, Tanmoy Samanata, at IIA for offering me help and guidance with the nitty gritty details of IDL. Last but not the least, I would like to thank my family: my parents for supporting me spiritually, emotionally throughout my life. I also would like to thank my friends at IISER Pune, for being there with me through thick and thin.

Contents

List of Figures

1 Introduction

The Sun has long been the focus of humanity's curiosity. Throughout the history of civilisation, it has brought about new religions, philosophies, and sciences. It in a way started the modern sciences, when Copernicus formulated his heliocentric theory. It has changed our understanding of our place in the Universe and allowed us to push forward the frontiers of stellar astronomy. Although our understanding of the Sun is nowadays more advanced, the curiosity we hold for it has not faded since the time of our ancestors. Now, we understand the Sun is a star similar to any other in its class, currently going through an 11 year cycle of activity, currently in the 24^{th} cycle, that is extremely rich in physical complexity. The study of such complex phenomena has yielded immeasurable advances in many areas of physics such as spectroscopy, plasma physics, magnetohydrodynamics (MHD) and particle physics. Although some of these sciences have grown over decades (or even centuries) they are still incomplete. I hope this thesis will contribute to the continuing growth of these sciences and to the understanding of our nearest star. This chapter will begin with a short introduction to the basic physical concepts governing the behaviour of the Sun, including the layers of solar interior and atmosphere.

The Sun

The Sun is our nearest star, located 1.49×10^6 km from Earth at the centre of our solar system. Located on the main sequence of the Hetzpring-Russel (HR) diagram, of spectral class G2V, luminosity $L_\odot = (3.84 \pm 0.04) \times 10^{26}$ W, mass $M_\odot = (1.9889 \pm 0.0003) \times 10^{30}$ kg and radius $R_\odot = (6.959 \pm 0.007) \times 10^8$ m (Foukal, 2004). It was born approximately 4.6×10^9 years ago when a giant molecular cloud underwent gravitational collapse and began hydrogen nuclear fusion at its core (Bouvier & Wadhwa, 2010; Montmerle et al., 2006). The energy produced from this fusion resulted in enough pressure to counteract gravitational contraction and bring about a hydrostatic equilibrium, allowing the young star to reach a stability that is sustained today.

It is estimated the Sun will maintain this stability for another 4.8 billion years from now, at which point, it will move off the main sequence and into a red giant phase (Sackmann et al., 1993). During this later part of its life, begin nuclear burning of heavier elements such as helium, carbon and oxygen and it will grow in size to 200 times its current radius. Once carbon burning in the core has ceased it can no longer sustain nuclear fusion of heavier elements, resulting in a gravitational instability that will eventually lead to a stellar nova. This nova will result in the loss of the outer envelopes and ultimately the Sun's death, leaving behind a compact and dense white-dwarf. Until then, the Sun will remain on the main sequence in a regular state of hydrogen fusion in its core. The energy released during this process is the ultimate source of light and all energetic activity that we observe from Earth and beyond. It is the reason of our very existence. Before we can understand how this energy manifests in the solar atmosphere as a variety of energetic phenomena, it is important to understand how the energy is generated and transported through its interior and finally released into interplanetary space.

Solar Interior: Energy generation and Propagation

The theoretical treatment of how the solar interior is structured and how it behaves is known as the 'standard solar model' or SSM. The SSM is a grouping of theories that describe how the Sun was formed, how it maintains its stability, how it generates energy, and how this energy is transported through its interior and released at the surface. Essentially there are four main aspects of SSM for describing the behavior of the solar interior. The SSM firstly states that the Sun was born from the gravitational collapse of a primordial gas of hydrogen, helium, and traces of other heavy elements (Sackmann et al., 1993). Secondly, it maintains its structural stability via a hydrostatic equilibrium such that the gravitational force is balanced by a pressure gradient ($\nabla P = -\rho g$) at each radial distance inside the star. The third main aspect of the SSM involves the source of the Sun's energy. The fourth aspect being the propagation of this energy from its core to the surface.

The pioneering neutrino physics experiments of the 1970s confirmed that the energy source is a hydrogen fusion process, namely the proton-proton or 'pp' chain, in the solar core (Davis et al., 1968). In this process, four protons are fused to form a helium nucleus. This can occur in a variety of ways, but at the Sun's core temperature of 15 MK, the dominant reaction is the pp I chain given by

$$ {}^{1}_{1}\mathrm{H} + {}^{1}_{1}\mathrm{H} \rightarrow {}^{2}_{1}\mathrm{H} + e^{+} + \nu_{e} \tag{1.1} $$

$$ {}^{2}_{1}\mathrm{H} + {}^{1}_{1}\mathrm{H} \rightarrow {}^{3}_{2}\mathrm{He} + \gamma \tag{1.2} $$

$$ {}^{3}_{2}\mathrm{He} + {}^{3}_{2}\mathrm{He} \rightarrow {}^{4}_{2}\mathrm{He} + 2\,{}^{1}_{1}\mathrm{H} \tag{1.3} $$

where ${}^{1}_{1}\mathrm{H}$ is a hydrogen nucelus, ${}^{2}_{1}\mathrm{H}$ is deuterium, ${}^{3}_{2}\mathrm{He}$ is tritium, ${}^{4}_{2}\mathrm{He}$ is helium, e^{+} is a positron, ν_e is an electron neutrino, and γ is a gamma ray photon. Reactions (1.1) and (1.2) must happen twice for (1.3) to occur. Taking this into account, the entire process may be summarised as

$$ 4\,{}^{1}_{1}\mathrm{H} \rightarrow {}^{4}_{2}\mathrm{He} + 2e^{+} + 2\nu_{e} + 2\gamma \tag{1.4} $$

liberating 4.2×10^{-12}J of energy per reaction, with $\sim$2.4% of the energy carried away by the neutrinos. This particular form of the pp-chain (pp I) occurs in 86% of the cases in solar core nuclear fusion (Turck-Chièze & Couvidat, 2011). However, there are other reactions capable of producing He from H catagorized into pp II, pp III etc, which each involve production of ${}^{7}_{4}\mathrm{Be}$ and ${}^{8}_{5}\mathrm{B}$; these were actually the first to be confirmed despite these reactions being less common than pp I (Davis et al., 1968).

The neutrino experiments together with the SSM provide much of what we know about the solar energy generation and the solar core. They imply a temperature of 15.6×10^6 K and density of $1.48 \times 10^2\,\mathrm{g\,cm^{-3}}$ at solar centre, where fusion occurs over a height range of $0.0 - 0.25\,R_\odot$ (Figure 1.1). These fusion processes occur over $0.0 - 0.25\,R_\odot$ (Figure 1.1), which defines the solar core. Outside the core the temperature drops to a value such that fusion ceases. While thermonuclear fusion is the third aspect of the SSM involves the generation of solar energy, the fourth aspect involves exactly what happens to this energy once it is generated i.e., it describes an energy transport mechanism.

Beyond $0.25\,R_\odot$ the temperature drops to 8 MK, such that fusion stops but only free protons and electrons exist. In this environment, the photons continuously scatter off of free particles, undergoing a random walk toward the surface over a distance of $0.25 - 0.7\,R_\odot$. This region is known as the radiative zone and has densities of $2 \times 10^1 - 2 \times 10^{-1}\,\mathrm{g\,cm^{-3}}$, resulting in a small photon mean free path (mfp) of 0.9 cm. The photons proceed towards the solar surface over a very long time scale, taking on the order of 10^5 years to traverse this region (Mitalas & Sills, 1992). The occurrence of such a radiative energy transport results in a temperature gradient given by

$$\frac{dT}{dr} = -\frac{3}{16\sigma}\frac{\kappa\rho}{T^3}F_{rad} \tag{1.5}$$

The above equation is actually a diffusion equation for radiation. If one takes the divergence of both sides and you have $\nabla = \kappa^{'\nabla^2 T}$, with κ' being the diffusion coefficient given by $\kappa^i = \frac{16\pi^3}{3\kappa\rho}$ e.g., the opacity controls to mean free path, and hence the diffusion of photons. where σ is the Stefan-Boltzman constant, κ is the mass extinction coefficient (opacity per unit mass), ρ is mass density, T is temperature, and F_{rad} is the outward radiative flux (Foukal, 2004). This implies that for a particular outward flux, if the opacity increases, a steeper temperature gradient is required to maintain such a flux. At $0.7\,R_\odot$ the temperature drops to 1 MK allowing protons to capture electrons into a bound orbit. The existence of electrons in atomic orbit results in a dramatic increase in opacity of the plasma (Turck-Chièze & Couvidat, 2011) and hence the temperature gradient increases. The increased temperature gradient required to sustain the energy flow may lead to the onset of a convective instability beyond $0.7\,R_\odot$ toward the solar surface. This instability will occur if the temperature gradient in the star is steeper than the adiabatic temperature gradient

$$\left|\frac{dT}{dr}\right|_{star} > \left|\frac{dT}{dr}\right|_{adiabatic} \tag{1.6}$$

This is known as the Schwarzchild criterion, and it is fulfilled from $0.7 - 1\,R_\odot$, a region known as the convection zone. The temperature and density drop as height increases and finally reaches T$\sim$ 6000 K and mass densities of $\rho \sim 1 \times 10^{-8}\,\mathrm{g\,cm^{-3}}$ at $1\,R_\odot$. Much of what we know about the depth, temperature, and density of the convection zone comes from a fine-tuning of the standard solar model, such that the model reproduces the results of helioseismology observations. Helioseismology makes use of the fact that the Sun acts as a resonator for acoustic waves which manifest as detectable oscillations in the doppler shift of photospheric Fraunhofer lines. These acoustic waves are referred to as pressure or p-modes, and a variety of wavelengths exist, generally with a period of approximately 5 minutes (Turck-Chièze & Couvidat, 2011). Convection ceases at $1\,R_\odot$, where the environment makes a sudden transition to convectively stability. At this point the opacity drops and energy is released in the form of radiation, demarcating the start of

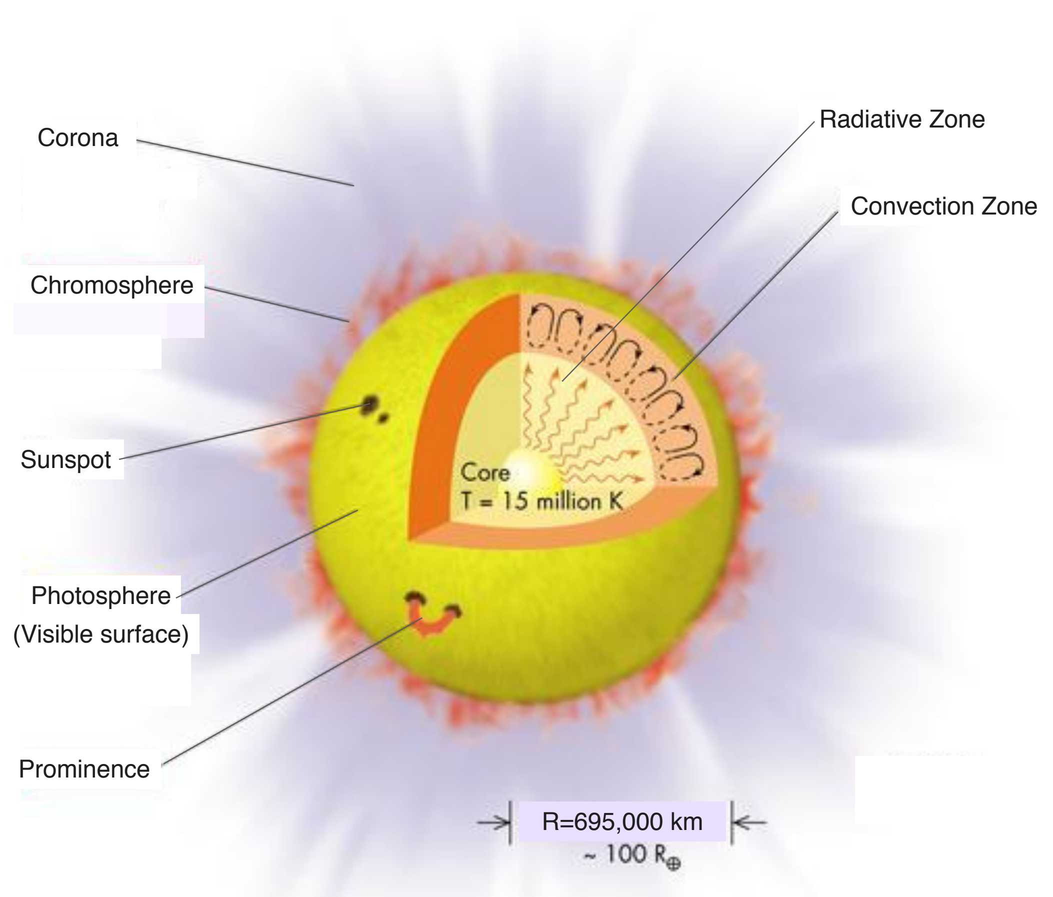

Figure 1.1: The structure of the solar interior and atmosphere, including the core, radiative zone, convective zone, photosphere, chromosphere, and corona. While the various interior zones are demarcated in terms of the dominant energy transport mechanism, the layers of the solar atmosphere are usually demarcated by temperature changes as height above the solar surface increases. The temperature ranges from $\sim$6000 K in the photosphere to above 1 MK in the corona.

the solar surface, known as the photosphere.

Different wavelengths probe different depths in the interior, and can provide information on density, sound speed and temperature. The shorter wavelengths in the mode propagate into the solar convection zone and experience a total internal reflection at a shallow depth, while longer wavelengths can penetrate into much deeper layers. Hence depending on the period observed, the oscillations provide a probe of the dynamical properties at a particular depth inside the sun. Analysis of these oscillatory modes has revealed that the differential rotation that is observed at the solar surface continues down into the convection zone, however the deeper radiative zone rotates as a solid body. In going from the convection zone to the radiative zone there is a sudden dramatic transition in the rotational dynamics of the solar interior (Thompson et al., 2003). This sudden change occurs in a region sandwiched in between the radiative and convective zones, known as the tachocline. The study of this layer is extremely active as it is believed to play an important role in the generation and evolution of the solar magnetic field.

One such property closely monitored is the sound speed, which is seen to match the predicted sound speed based on the standard model. However, the observation and prediction show the biggest deviation at a depth of $0.3\,R_{\odot}$, which is the region where the radiative zone transitions to the convective zone. This obviously implies that SSM is lacking in its description of how the solar interior is stratified at this depth. This partly due to the fact the SSM does not take into account differential rotation. The solar surface rotates faster at the equator than it does at the poles i.e., angular velocity is stratified with latitude. Helioseismology has revealed that such differential rotational continues to the bottom of the convection zone. In the deeper radiative zone and core the Sun rotates as a solid body. There is a dramatic change in the internal dynamics when transitioning from convective to radiative zones. As predicted by sound speed measurements and differential rotation, the region sandwiched in between radiative and convective zones is and extremely important boundary. It is known as the tachocline, and the dynamics of this thin layer is believed to play and extremely important role in the generation and evolution of the solar magnetic field (Thompson et al.,

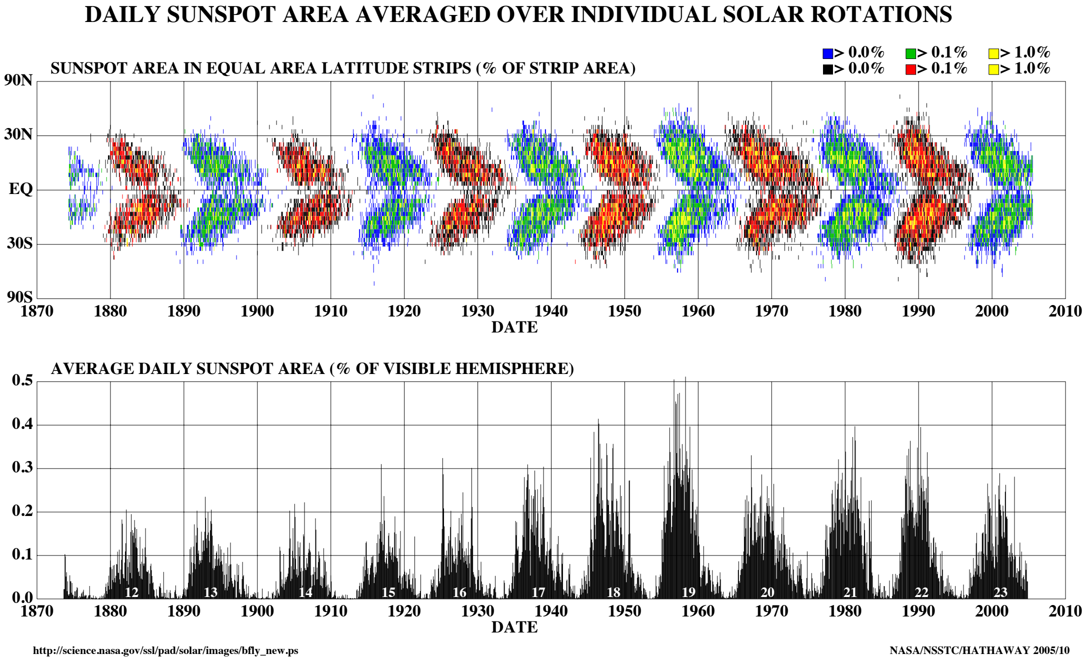

Figure 1.2: Top: The latitude of sunspots as a function of time, known as the 'butterfly diagram'. During the rise phase of each cycle the sunspots have a latitudinal distribution of ±30° from the equator. As the solar cycle progresses, sunspots emergence takes place at an increasingly lower latitude. Bottom: Sunspot area as a function of time. The spot area, or number of spots, is a proxy for solar magnetic activity which approximately follows and 11 year periodicity. *Image courtesy of http://science.nasa.gov.*

2003).

Solar Magnetic Field

The solar magnetic field plays a dominant role in the energetic activity occurring in the solar atmosphere. At solar activity minimum the solar magnetic field has a poloidal dipolar structure. However as the activity cycle progresses towards a maximum, the field gains a strong toroidal component, making it far more dynamic and complex. This complex toroidal component manifests at the surface as sunspots, hence the number of sunspots on disk has been used as a proxy for the magnetic activity cycle for over 100 years, often showing an approximate 11 year periodicity (Figure 1.2, bottom panel). At the beginning of the cycle sunspots tend to appear on disk with a latitudinal distribution of $\pm 30°$ of the equator. As the cycle progresses, sunspots appear at lower and lower latitude (known as Spörer's law), until they eventually disappear at the end of a cycle. Sunspot latitude with respect to time is shown in Figure 1.2, top panel, and is known as the 'butterfly diagram'.

Sunspots in there simplest case emerge as a dipolar structure, (Aschwanden, 2004) with the leading spot being closer to the equator, such that the dipole is titled relative to the solar equator (Joy's law). In a given hemisphere, the leading sunspot and trailing spot have opposite polarities, with the polarities reversed in the other hemisphere (Hayle's law). The trailing polarity can often be more fragmented and dispersed than the leading polarity. Despite sunspots generally having a dipolar structure, spot groups can be far more complex, having a complex multipolar structure these spots are usually the more active ones. Over the course of a solar cycle, the Sun changes polarity at the time of sunspot maximum. For example, an overall dipolar configuration of North-South will become South-North, another cycle will bring it back to North-South once more (one full magnetic cycle takes 22 years). The complex behavior of the solar magnetic field over an 11 year activity cycle, during which the dipole reverses sign, is generally explained by solar dynamo theory. This is a magnetohydrodynamic theory that involves large-scale flow patterns of the solar interior that act to both induct and diffuse the magnetic field such that it produces the familiar 11 year magnetic activity cycle (Charbonneau, 2010) and other observed phenomena (Spörer's, Joy's, and Hale's laws). The theory is incomplete but there is an

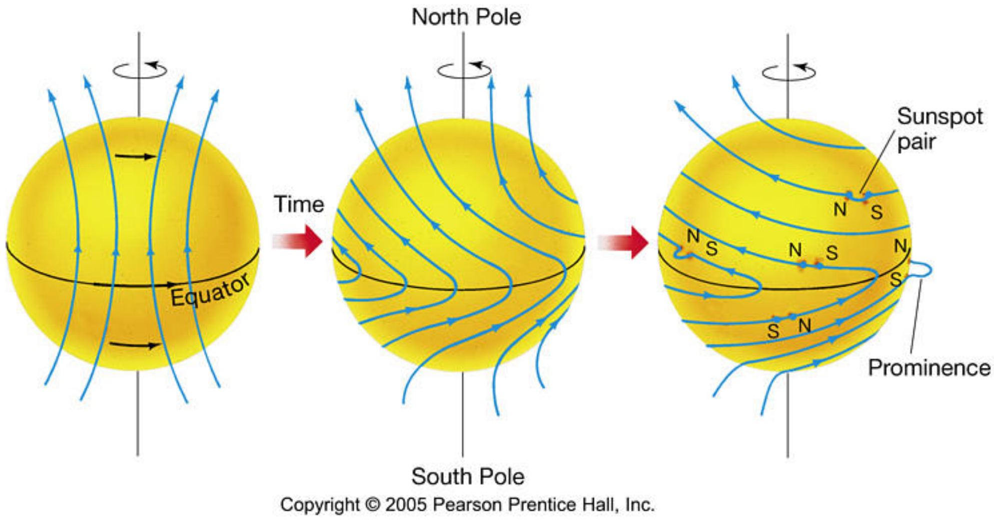

Figure 1.3: Differential rotation and flux freezing result in the poloidal dipolar magnetic field, generated by dynamo action, to be dragged around in a toroidal direction, an action known as the omega effect. Buoyancy of the field lines results in them rising and twisting, known as the alpha effect, eventually surfacing to become bipolar fields that extend far into the corona.

accepted paradigm on the general behaviour of the magnetic field throughout the cycle, known as the Babcock model. Magnetohydrodynamics (MHD) is employed to describe such that the magnetic induction equation and velocity field equation (equation of motion) are solved in numerical models to produce a toroidal field from a poloidal one, a process known as the Ω-effect. The theories must adhere to the constraints provided by observations of the sunspot cycle (Spörer's, Joy's, and Hale's laws), and also helioseismology observations of how the interior is structured.

Although solar dynamo theory is an active area of research and a number of questions still remain, the generally accepted paradigm for the activity cycle was first proposed by Babcock (1961). The mechanism involves differential rotation of the solar convection zone that tends to drag the field from a poloidal position into a toroidal one (known as the Ω-effect), eventually winding the field around the solar axis into a stressed state, see Figure 1.3. The main storage of this wound field is in the region below the convection zone known as the tachocline. The stored field eventually gets wound into twisted magnetic structures called 'flux-ropes'. A continuous build up of magnetic field strength in these ropes increases their magnetic pressure and they become convectively unstable and rise to the surface. When the field eventually surfaces it creates sunspots in the photosphere and a complex magnetic structure in the solar atmosphere known as an active region (Fan, 2009). The active regions themselves may be sheared, twisted and generally evolves to build huge amounts of potential energy. The conversion of the potential energy to thermal and kinetic energy is what causes explosive events such as flares and CMEs.

Over the course of the solar cycle a number of flows in the photosphere and deeper layers are responsible for a transport of magnetic flux that eventually leads to the solar dipole flip. For example, the northern heliographic pole is initially dominated by north magnetic flux; a 'meridional flow' (poleward flow) carries south magnetic flux from equatorial latitudes to the northern heliographic pole. This slow build up of southern magnetic flux eventually dominates the pre-existing northern flux. The opposite happens at the southern heliographic pole. Hence, over the course of the solar cycle, the transport of magnetic flux from equator to poles causes a change in magnetic pole sign at each pole. This leads to an overall flip in the dipole field of the Sun, and also brings the field from a complex toroidal state (at solar maximum) back to to an ordered dipoler state (at solar minimum).

Solar Atmosphere

The solar atmosphere begins above the visible surface of the Sun, known as the photosphere. At this point, the Sun become optically thin to visible radiation and light escapes from this surface. Beyond this visible surface is the solar chromosphere, and the corona, which eventually becomes the solar wind. Each of these layers is home to a complex variety of phenomena, and each layer, with its accompanying attributes, is described here.

Photosphere

As mentioned, the photosphere begins where the atmosphere become optically thin to visible radiation. Visible light in this instance is usually taken to mean light with a wavelength of 5000 Å (1 Å=0.1 nm), hence the emergent light from the photosphere is taken to come from the surface at which $\tau_{5000} = 2/3$, where τ is the optical depth. The optical depth of 2/3 is a consequence of the Eddington-Barbier approximation, and says that emergent flux F_ν from the photosphere is given by

$$F_\nu = \pi B_\nu(\tau = 2/3) \tag{1.7}$$

e.g., the emergent flux is given by π times blackbody intensity at an optical depth of 2/3, where blackbody intensity B_ν is given by Planck's law

$$B_\nu = \frac{2h\pi\nu^3}{c^2}\frac{1}{\exp(h\nu/k_B T) - 1} \tag{1.8}$$

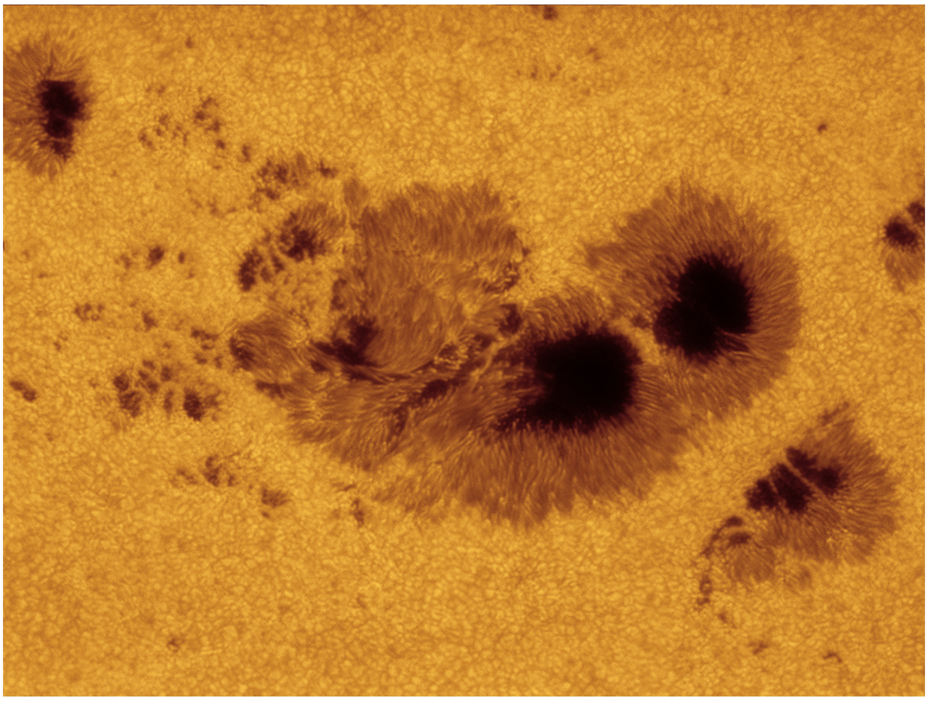

Figure 1.4: Sunspots are planet-sized, dark patches in the photosphere. They appear dark because they are slightly cooler than the surrounding surface.

where h is Planck's constant, ν is frequency, c is the speed of light, k_B is Boltzmann's constant, and T is temperature. Integrating Equation 1.8 over frequency results in $F = \sigma T^4(\tau = 2/3)$, showing the frequency integrated flux is proportional to the temperature at $\tau = 2/3$, hence the effective temperature of solar blackbody radiation is $T_{eff} = T(\tau = 2/3) = 5800\,\mathrm{K}$. Solar radiation at visible wavelengths is most closely characterised by a blackbody of temperature 5800 K, although the brightness temperature T_B of the photosphere can deviate from this value, since not all frequencies emerge from the same physical depth.

The visible appearance of the photosphere reveals a small scale granular structure, with granules of typical size scale of 1000 km and a lifetime of 5–10 minutes. The granules typically show bright centers (regions of upflow) surrounded by darker intergranular lanes (regions of downflow). Doppler measurements reveal that granule centres have a positive (upward) velocity of up to $\sim 1\,\mathrm{km\,s^{-1}}$, with intergranular lanes having a negative (downward) velocity. Such upward and downward flow indicates that granulation at the photosphere is the surface manifestation of convective activity in the deeper layers of the interior (Schrijver & Zwaan, 2008). As well as the conspicuous granulation there is also 'supergranulation' which has the same mechanism as the granules, but of a much larger size of $10,000 - 30,000\,\mathrm{km}$. Apart from granules and supergranules, the most conspicuous features of the photosphere are sunspots, regions of concentrated magnetic flux that have penetrated from the solar convective zone into the solar atmosphere. The spots have a temperature of $\sim$4000 K, which is cooler than the typical solar blackbody temperature of 5800 K. Typical magnetic field strengths in sunspots are on the order of kilo-Gauss, while quiet regions of the photosphere are permeated by fields with tens of Gauss.

Temperature and density diagnostics of the photosphere and above are usually determined through an analysis and modeling of Fraunhofer lines e.g., the Hα and CaII H and K lines (Fontenla et al., 1988; Gabriel, 1976; Vernazza et al., 1981). The temperature and density diagnostics as a function of height above the photosphere is shown in Figure 1.5. After the $\tau_{5000} = 1$ level the temperature drops to a minimum of $\sim$4400 K at $\sim$400 km above the photosphere before rising again, eventually undergoing a rapid increase at $\sim$2000 km. The region between the temperature minimum up to the height at which temperature begins to rise rapidly is the next layer of the atmosphere beyond the photosphere, known as the chromosphere.

Dark absorption features, such as the Hα and CaII H and K lines Fraunhofer

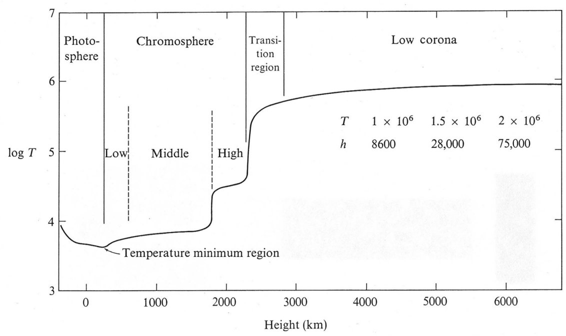

Figure 1.5: Temperature and density variation in the solar atmosphere constructed from the models of Fontenla et al. (1988); Gabriel (1976); Vernazza et al. (1981). Figure from Aschwanden (2004).

lines, are superimposed on the photospheric blackbody and provide a useful diagnostic of temperature with respect to height (Fontenla et al., 1988; Gabriel, 1976; Vernazza et al., 1981), whereby a model temperature and density profile of the solar atmosphere is used to calculate the emergent line intensity, using radiative transfer theory. This temperature and density profile is adjusted until the modeled emergent intensities match the observed ones. The results of this these models is shown in Figure 1.5. After the $\tau_{5000} = 1$ level the temperature drops to a minimum of $\sim$4400 K at $\sim$400 km above the photopshere before rising again, eventually undergoing a rapid increase at $\sim$2000 km. The region between the temperature minimum up the height at which temperature begins to rise rapidly is the next layer of the atmosphere beyond the photosphere, known as the chromosphere[1].

[1]These boundaries can vary, depending on the phenomenon observed e.g., spicules are chromospheric phenomenon which can extend far beyond the upper boundary of $\sim$2000 km

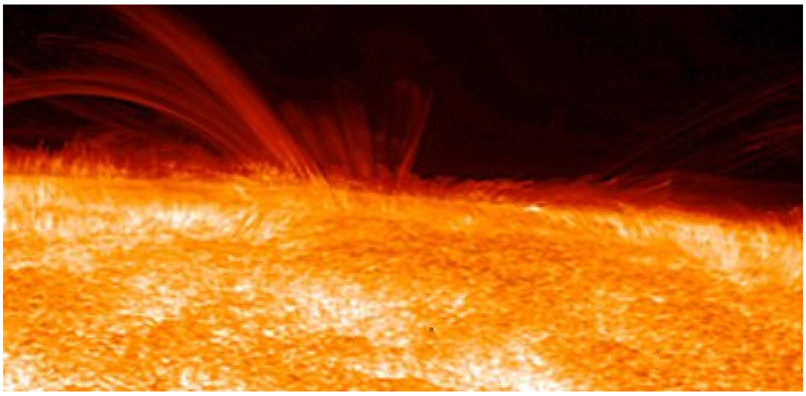

Figure 1.6: Chromosphere as seen from IRIS. . One can see the tiny fibril like structure, called the spicules. Also one can see the jet like structure extending outward.

Chromosphere

As predicted by the models of Fontenla et al. (1988); Gabriel (1976); Vernazza et al. (1981), at ~400 km above the $\tau_{5000} = 1$ surface the temperature drops to a minimum of ~4400 K. Beyond this minimum the temperature begins to rise again, demarcating the beginning of the chromosphere. This layer of the atmosphere is generally accepted to extend to a height at which temperatures reach 20,000 K, however temperatures as high as $\sim 1 \times 10^5$ K are sometimes attributed to chromospheric heights, hence it is observable at visible lines such as Hα and CaII H and K, and ultraviolet (UV) wavelengths such as Ly-α at 191.5 nm, the strongest line in the solar atmosphere.

The chromosphere is primarily observed through the the Fraunhofer Hα and CaII H and K lines. These lines in particular provide a good diagnostic of the chromospheric environment over a large height range since different sections of the lines are formed over various heights. By viewing the Sun at or near the cores of the lines we may view different height s in the chromospheric part of the atmosphere. The chromosphere, when observed using the Ca lines, shows a highly non-uniform structured and structured appearance. The structure is made up of dark cells with a diameter of approximately 30,000 km, with bright boundaries of the cells making up a network of bright features known as 'the chromospheric network'. These network boundaries consisting of bright points are positions of near vertical magnetic field with a strength of kilo Gauss. This chromospheric network is directly related to the supergranular structure as observed in the chromosphere i.e., the supergranular flows in the photosphere tend to transport field toward the boundaries of the network where they may coalesce and strengthen. These regions of strong magnetic field facilitate heating in the upper chromosphere and hence show up as regions of enhanced emission (by magnetic acoustic oscillations) in the centers of the CaII K, for example (McAteer et al., 2002). Enhanced emission in the internetwork regions (supergranule centres) show up as bright points when viewing Ca H2V and are now accepted to be formed by heat of the mid-low chromosphere by acoustic shocks (Carlsson & Stein, 1997) Beyond the temperature minimum there is a broad temperature plateau between $\sim 1000-2000$ km, after which the temperature starts to increase dramatically. Similar to the photosphere, supergranulation is present in the chromosphere, indicating that this layer of the atmosphere is magnetically structured with concentrations or bundles of magnetic fields confined to isolated regions in the intergranular lanes. These concentrations of magnetic field are believed to play a role in chromospheric heating (Carlsson & Stein, 1997). Other dynamic features of the chromosphere are spicules, as shown in figure 1.6 small but ubiquitous jets of plasma reaching about $\sim 10^4$ km, traveling into the atmosphere at $100\,\mathrm{km\,s^{-1}}$ and lasting tens of minutes. These are believed to also play a role in the ejection of plasma and heating of the solar atmosphere (De Pontieu et al., 2004). Although spicules begin in the chromosphere they penetrate into higher layers of the atmosphere where temperature increases further. When the temperature reaches 20,000 K the extremely prominent Ly-α emission line is formed, with a wavelength of 191.5 nm, and this is accompanied by other prominent ultraviolet lines such as those of C IV, formed at temperatures of ~110,000 K. The sharp gradient in temperature at 2000 K is generally known as the transition region.

Transition Region

The layer sandwiched in between the chromosphere and the corona is the transition region. It is characterised by temperatures of $\sim 10^5$ K, has the steepest temperature gradient in the solar atmosphere and is extremely narrow at just 200 km in width. The SDO/AIA 304 Å image shows the chromosphere and transition region, in which the supergranular network can still be seen (Figure 1.8). The 171 Å image shows the upper transition region and corona. The network has just about disappeared at this height. As described, the network outlines the magnetic structure of the atmosphere, hence the magnetic field goes from ordered and concentrated in the chromosphere to more ubiquitous and complex in the corona, and is sometimes termed the 'magnetic canopy', as shown in Figure 1.7.

Acoustic shocks heat the low-mid chromosphere in the internetwork region (supergranule centres) and show up as bright points when viewing CaII K lines. But the magnetic bright points (at the network boudnary) in higher altitude lines are thought to be upper chromosphere where MHD waves heat the environment, as evidenced by brightening in Ca II K core.

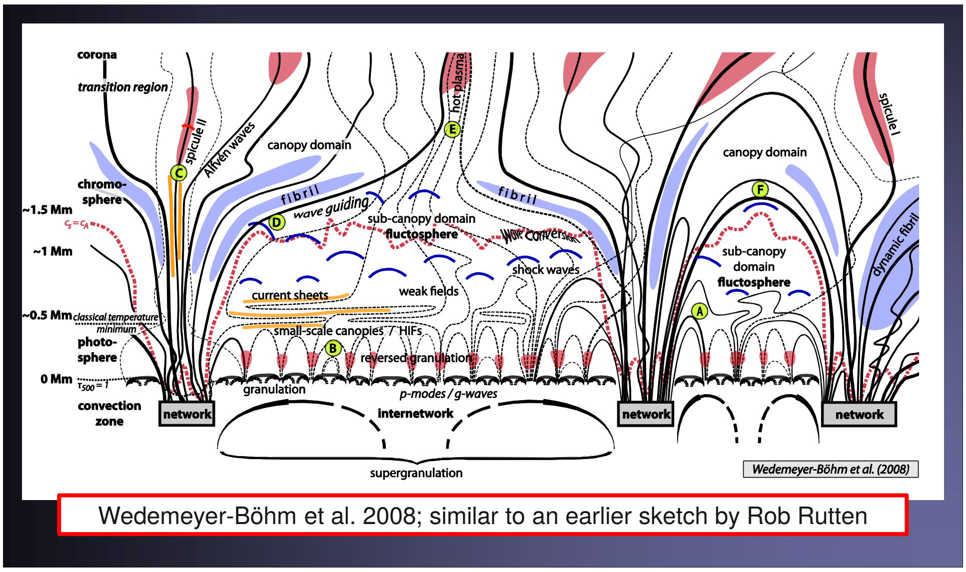

Figure 1.7: Magnetic canopy, one can see the various structures like granulation, intergranulation and networks and internetworks.

Details in the chromosphere are imaged using the lines of H-alpha and Ca II H and K. These Fraunhofer lines are formed over a large range in heights. The H-alpha line is photoelectrically controlled, so the decrease in line intensity is to do with the source function being lower because of a lack of photospheric photons at that height the line centre 'samples Ca II H and K is collisionally controlled so the decrease in line intensity is to do with the source function being lower because of the dropping temperature Different regions in the Ca II H and K lines sample different heights in the photosphere/chromosphere. Tuning imagers to different parts of these lines allows imaging of chromosphere at different heights.

Chromospheric lines not in the visible are the Mg h and k Fraunhofer lines, also collisionally controlled. There is also the Ly-alpha emission line, formed at 20,000 K, which is optically thin. There is C IV, formed at 110,000 K, at this point we are starting to sample to transition region.

Note: Fraunhofer lines such as Calcium H and K are not as simple as a case of a cloud of cooler gas absorbing lines from a hot radiations source. The Fraunhofer lines are a consequence of the Eddington-Barbier Approximation i.e., that the emergent intensity is equal to the source function at an optical depth of 2/3. So in the centre of the line the opacity goes up and optical depth 2/3 is higher in the atmosphere where the plasma is cooler. Hence, the line is darker at the centre (due to the smaller source function at the cooler temperature).

Corona

The outermost layer of the solar atmosphere is known as the solar corona, beginning at ∼2500 km above the photosphere. It has an electron number density of $10^9\,\mathrm{cm}^{-3}$ at its base in quiet regions, decreasing to $10^6\,\mathrm{cm}^{-3}$ at distance of $1\,R_\odot$ from the solar surface. The models of Fontenla et al. (1988); Gabriel (1976); Vernazza et al. (1981) reveal that beyond the transition region (∼2500 km) the temperature in the corona reaches well over 10^6 K. Such high temperatures allow the formation of emission features that belong to highly ionized heavy elements, for example Fe IX, up to as high as Fe XXIV. The presence of these highly ionized species (and many others) show that the corona has temperatures in the $1-2$ MK range in quiet regions, active regions may exhibit temperatures in the range of $2-6$ MK, while coronal holes may be lower than 1 MK. The temperatures of a flaring active region can be even higher than this, reaching tens of MK. The presence of highly ionized species of heavy elements means the low corona may be primarily observed in the ultraviolet and X-ray. When viewed at these wavelengths, the corona appears highly structured, showing concentrations of bright

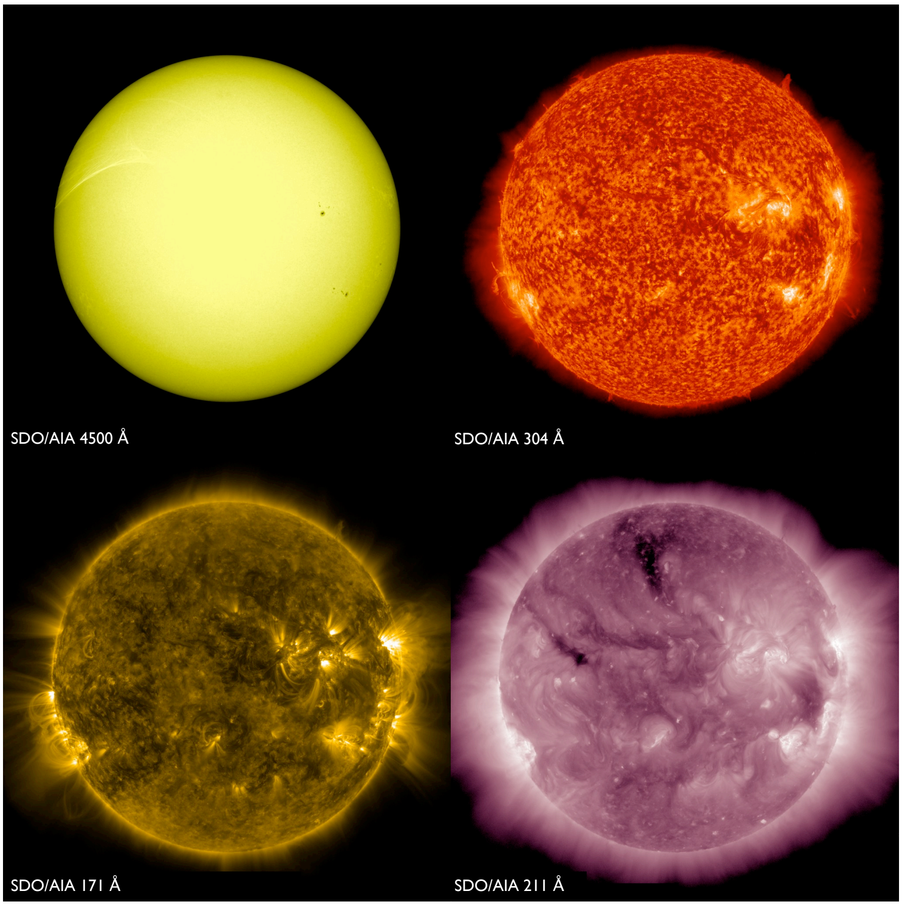

Figure 1.8: Atmospheric Imaging Assembly (AIA) observations of the photosphere (4500 Å), chromosphere (304 Å), transition region (304 Å,171 Å), and corona (171 Å, 211 Å). Bright regions are concentrations of magnetic field known as active regions.

loops known as active regions (Fig. 1.8).

Ultraviolet wavelengths allow observations of the very low corona, perhaps to only a few scale heights. However, the most extensive observations of the corona are in the visible, generally known as the 'white-light' corona (Figure 3.1). The corona's white-light radiation is primarily due to scattering of photospheric light by particles and dust grains. The component which is due to Thomson scattering by free electrons is known as the *Kontinuierlich* or K-corona. The spectrum of this light is the same as the photospheric continuum except for the absence of Fraunhofer lines. These lines are 'washed-out' of the spectrum due to thermal Doppler broadening of the high-velocity free electrons that scatter the light. The emission is optically thin, so the intensity is due to the number of scattering agents along the line of site (this is explained in detail in Chapter 3, Section 3.1). The K-corona dominates white-light emission from low atmosphere to $\sim 4R_{\odot}$. After this height, there is an increasing contribution from Rayleigh or Mie scattering from interplanetary dust grains, known as the the Fraunhofer or F-corona. Since these dust grains move at a much slower velocities than the electrons, they do not wash out the Fraunhofer lines of the photospheric spectrum. The F-corona extends far beyond Earth and a can be viewed in the night sky as *Zodiacal light.*

Plumes

The solar corona is home to a variety of dynamic features, that are morphologically distint. One of such features are the plumes. The plumes have been observed since the early days of white light images of the eclipse (Saito, 1958). These are classified as two types one is the polar plumes which were the first to be discovered, that can be seen as fine structures on the pole of the Sun in the white light image, during eclips. The otehr being the on-disk plume. Historically the ones on the poles (Polar plumes) have garnered more attentiona and fascination from the solar physics community because of its possible role in the solar wind. Plumes being the open magnetic field structures are responsible for carrying away the charged particles.

Thesis Outline

Firstly, I will discuss about the Sun and its properties, energy generation and transfer, the next chapter focuses on the instruments used and the basics of obtaining images for scientific studies. The next chapter deals with the magntohydrodynamic description, and discusses the MHD waves. The final chapter deals with the analysis and observation of the waves in an open magnetic field structure.

2

Magnetohydrodynamics

This chapter introduces the theory used to study the phenomenon in corona. Since the corona is a plasma, the theoretical framework under which all coronal phenomena are treated is in plasma physics and a fluid description of plasmas known as magnetohydrodynamics (MHD). Although the validity of MHD applicability is not very rigorous in corona, it is still the best description of it. Therefore, both the MHD equations is presented in this chapter, followed by a section on the wave propagation in solar corona.

Magnetohydrodynamics

Maxwell's Equations

Since plasmas are an electrically conducting fluid which may interact with electromagnetic fields, Maxwell's equations are an essential starting point for all plasma theory. Maxwell's equations form a closed set of four unknowns and four equations describing relationships between the electric field $\mathbf{E}$, the magnetic field $\mathbf{B}$, the current density $\mathbf{j}$, and the charge density ρ_q

$$\nabla \cdot \mathbf{E} = \frac{\rho_q}{\epsilon_0} \tag{2.1}$$

$$\nabla \cdot \mathbf{B} = 0 \tag{2.2}$$

$$\nabla \times \mathbf{E} = -\frac{d\mathbf{B}}{dt} \tag{2.3}$$

$$\nabla \times \mathbf{B} = \mu_0 \mathbf{j} + \frac{1}{c^2}\frac{d\mathbf{E}}{dt} \tag{2.4}$$

μ_0 and ϵ_0 are the magnetic permeability and electric permittivity of free space, respectively, and all bold face quantities represent vector variables. At velocities typically found in a plasma Equation (2.4), Ampére's law, reduces to

$$\nabla \times \mathbf{B} = \mu_0 \mathbf{j} \tag{2.5}$$

where the displacement current is no longer included. Maxwell's equations describe electromagnetic behaviour and they constitute an important part of the fluid description of plasmas. Before we define fluid description a brief discussion of plasma kinetic theory, from which the fluid theory is derived, is provided here.

Magnetohydrodynamics

The conservation principles derived from moments of the Boltzmann equation are firstly the mass conservation equation

$$\frac{D\rho}{Dt} = -\rho\nabla\cdot\mathbf{v} \tag{2.6}$$

where ρ is mass density, $\mathbf{v}$ is bulk flow velocity, t is time, and D represents a Lagrangian derivative ($D/Dt = \partial/\partial t + v\cdot\nabla$). This expression simply states that the rate of change of particles into or out of a volume is controlled by the fluid flow into and out of the volume. It has units of $\mathrm{g\,cm^{-3}\,s^{-1}}$.

Secondly, the momentum conservation equation is

$$\rho\frac{D\mathbf{v}}{Dt} = -\nabla p + \nabla\cdot\mathbb{T} + \mathbf{j}\times\mathbf{B} + \mathbf{f} \tag{2.7}$$

where p is thermal pressure, $\mathbf{j}$ is the current density, $\mathbf{B}$ is the magnetic field, $\mathbf{f}$ are all body forces e.g., gravity, and $\mathbb{T}$ is a stress tensor. This equation shows that the change in momentum of a fluid may be due to a pressure gradient, the 'j cross B' or Lorentz force, gravity, and any stresses in the plasma. For an incompressible fluid only shear stresses are included, such that $\nabla\cdot\mathbb{T} = \rho\nu\nabla^2\mathbf{v}$, where ν is the kinematic viscosity. For an isotropic fluid there is no shear stress and the momentum equation reduces to

$$\rho\frac{D\mathbf{v}}{Dt} = -\nabla p + \mathbf{j}\times\mathbf{B} + \mathbf{f} \tag{2.8}$$

Note that all terms in this equation have the form of a body force (force per unit volume), and integration over volume would render this equation an explicit version of Newton's second law ($m\mathbf{a} = \mathbf{F}$). Using Equation 2.5

$$\mathbf{j} \times \mathbf{B} = \frac{1}{\mu_0}(\nabla \times \mathbf{B}) \times \mathbf{B} = \frac{1}{\mu_0}(\mathbf{B} \cdot \nabla)\mathbf{B} - \nabla \frac{B^2}{2\mu_0} \tag{2.9}$$

The first term on the right is known as magnetic tension, and acts to restore a bent or curved field line to a straight line. The second term is known as the magnetic pressure and, like thermal pressure, any gradient in the field will produce a force. These two components of the Lorentz force play an important role in eruptions.

The third conservation equation is for energy

$$\rho \frac{De}{Dt} + p \nabla \cdot \mathbf{v} = \nabla \cdot (\kappa \cdot \nabla T) + \eta_e \mathbf{j}^2 + Q_\nu - Q_r \tag{2.10}$$

where

$$e = \frac{p}{(\gamma - 1)\rho} \tag{2.11}$$

is the internal energy per unit mass, γ is the ratio of specific heats, κ is the thermal conductivity, T is the temperature, η_e is electrical resistivity, Q_ν is heating by viscous dissipation, and Q_r is a radiative term. This equation demonstrates that any changes in the fluid internal energy are due to divergence in the flow field, conduction, Ohmic and vicious dissipation, and radiative losses.

The fluid momentum equations can be used to formulate Ohm's law for a plasma which describes the behaviour of current in terms of electric and magnetic fields and the fluid flow velocity

$$\mathbf{j} = \sigma(\mathbf{E} + \mathbf{v} \times \mathbf{B}) \tag{2.12}$$

This is a reduced version of the generalised Ohm's law and does not contains terms for the Hall effect, ambipolar diffusion, and electron inertia. The set of Equations (2.7 - 2.12), combined with an equation of state

$$p = nk_BT \tag{2.13}$$

results in a fully closed set of variables and equations, which can be solved for any fluid or electromagnetic property. In order to further simplify these set of equations the electric field $\mathbf{E}$ and current $\mathbf{j}$ are often eliminated by using Faraday's law in combinations with Ampére's and Ohm's law to produce the induction equation

$$\frac{\partial \mathbf{B}}{\partial t} = \nabla \times (\mathbf{v} \times \mathbf{B}) + \eta \nabla^2 \mathbf{B} \tag{2.14}$$

which describes the evolution of the magnetic field in terms of the plasma flow and the magnetic diffusivity $\eta = \eta_e/\mu_0$. The mass, momentum, internal energy equation, the induction equation, and the solinoidal constraint then define a fully closed system of resistive MHD equations in terms of the variables $(\mathbf{B}, \mathbf{v}, p, \rho)$

$$\frac{D\rho}{Dt} = -\rho \nabla \cdot \mathbf{v} \tag{2.15}$$

$$\rho \frac{D\mathbf{v}}{Dt} = -\nabla p + \frac{1}{\mu_0}(\nabla \times \mathbf{B}) \times \mathbf{B} + \rho g \hat{\mathbf{z}} - 2\rho\Omega \times \mathbf{v} \tag{2.16}$$

$$\frac{D\rho}{Dt} = -\gamma p \nabla \cdot \mathbf{v} + (\gamma - 1)\frac{\eta}{\mu_0^2}(\nabla \times \mathbf{B})^2 \tag{2.17}$$

$$\frac{\partial \mathbf{B}}{\partial t} = \nabla \times (\mathbf{v} \times \mathbf{B}) + \eta \nabla^2 \mathbf{B} \tag{2.18}$$

$$\nabla \cdot \mathbf{B} = 0 \tag{2.19}$$

It is also assumed here that the fluid is inviscid and not subject to any conductive or radiative energy losses or gains. Under this reduced set of equations, the ideal MHD equations are simply produced by setting $\eta = 0$ e.g., zero resistivity, which would eliminate the second terms on the right in Equations 2.22 and 2.23. Under such an assumption the ideal induction equation

$$\frac{\partial \mathbf{B}}{\partial t} = \nabla \times (\mathbf{v} \times \mathbf{B}) \tag{2.20}$$

may be used to show the 'frozen flux' condition. This shows that when $\eta = 0$ the field is advected with the plasma or the field is 'frozen-in' into the plasma and follows the flow velocity i.e., there is no 'slipping' of the magnetic field with respect to the fluid flow. On the other hand, a finite η leads to a variety of important diffusive effects for the magnetic field. The most important of these diffusive processes is magnetic reconnection, which plays an extremely important role in energetics of CMEs and flares.

Waves in Corona

Waves are ubiqitous in nature. The study of waves gives an insight about the physical conditions of the surrounding. The main restoring forces that play an important role in the atmosphere of the Sun are, (1) Gas Pressure, (2) Gravity and (3) Magnetic fields. A gas when is in disturbed from the stable equillibrium will start oscillatin under one of the three restoring forces leading to sound, gravity or Alfvén waves, respectively. There are three basic MHD waves, incompressible Alvén wave, slow and fast magneto-acoustic waves which are both compressible. To understand the propagation of waves in the Sun, we first study the wave propagation in uniform media (no discontinuity in the density, pressure, ormagnetic field). We use the basic MHD equations of continuity of mass, momentum energy and induction equation, listed in Equations 2.15 to 2.19. We will use the ideal induction equation 2.20. The electric current and the temperature have the following form

$$\mathbf{j} = \nabla \times \frac{\mathbf{B}}{\mu} \tag{2.21}$$

$$\mathbf{T} = \frac{mp}{k_B \rho} \tag{2.22}$$

To simplify these equations we work in a rotating frame with Sun, with angular velocity Ω. The rotation does not have significant effect on the Maxwellś equations, if the absolute speed $(\Omega \times r + v)$. The centrifugal force the can be incorporated in the gravitational term. The gravitational force is assumed to be constant along the ẑ direction, and the plasma is assumed to be adiabatic. Under a uniform magnetic field **B** with a uniform temperature($\mathbf{T_o}$)and the desity and pressure distributions governed by,

$$\rho_o(z) = const. \times \exp \frac{-z}{H} \tag{2.23}$$

$$p_o(z) = const. \times \exp \frac{-z}{H} \tag{2.24}$$

the equillibrium condition can be described by

$$-\frac{dp_o}{dz} = \rho_o g \tag{2.25}$$

where $H = \dfrac{p_o}{\rho_o g}$, the scale height of the medium. After of MHD under the linear perturbation of density $\rho = \rho_0 + \rho_1$, pressure $p = p_0 + p_1$, substituting these in the Equations 2.15 to 2.19, we get the single equation after taking $\frac{\partial}{\partial t}$ of equation 2.16. We get the equation

$$\frac{\partial^2 \mathbf{v_1}}{\partial t^2} = {c_s}^2 \nabla(\nabla \cdot \mathbf{v_1}) - (\gamma - 1) g \hat{z} (\nabla \cdot v_1) - g \nabla \nu_{1z} - 2\Omega \times \frac{\partial v_1}{\partial t} + (\nabla \times (\nabla \times B_0)) \times \frac{\mathbf{B_0}}{\mu \rho_0} \tag{2.26}$$

Using the plane solutions of Equation 2.26 as $\mathbf{v_1}(\mathbf{r}, \mathbf{t}) = \mathbf{v_1} \exp i(k \cdot r - \omega t)\mathbf{k}$ is the wavenumber. The period is described by $\frac{2\pi}{T}$. BY assuming the plane wave solutions one can replace $\frac{\partial}{\partial t}$ *as* $-i\omega$ *and* ∇ *as* $i\mathbf{k}$. we get a dispersion relation for $\mathbf{B_0} = 0$ by the following equation,

$$\omega^2 \mathbf{v_1} = {c_s}^2 \mathbf{k}(\mathbf{k_1}) + i(\gamma - 1) \hat{gz}(\mathbf{k_1}) + ig\mathbf{k}\nu_{1z} - 2i\omega\Omega \times \mathbf{v_1} \tag{2.27}$$

Magnetoacoustic waves originate when there is a coupling between the magnetic field and the pressure fluctuations. In this condition, one writes the Equation 2.27 with magnetic field in the absence of g or Ω.

Magnetoacoustic Waves

These originate as the interaction of the pressure and the magetic term in the equation 2.27. These are further classified into two cateories, demarcated by the speed of sound in that medium. The sound speed in a given medium is given by

$$C_s = \sqrt{\frac{\gamma p}{\rho}} \tag{2.28}$$

The dispersion relation, derived after taking B_0 in Equation 2.27, is $\frac{\omega^2}{k^2} = c^2(\frac{{v_s}^2 + {v_A}^2}{c^2 + {v_A}^2})$, for the magnetoacoustic waves.

Slow Magnetoacoustic Waves

If the speed of the wave is slower than that the speed of sound in the medium the wave is called slow magnetoacoustic wave.

Fast Magnetoacoustic Waves

If the speed of wave is more than the speed of the sound in the medium, the wave is said to of teh fast-magnetoacoustic type.

Alvén Waves

These are transverse waves generated by with restoring force being the magnetic tension. These will propagate along the field lines with speed given by $(\frac{\mathbf{B_0}^2}{\mu\rho_0})^{\frac{1}{2}}$ this expression is called Alvén speed (V_A),

$$V_A = \frac{B_0}{\sqrt{(\rho\mu_0)}} \tag{2.29}$$

The magnetic pressure generates longitudinal magnetic waves propagating across the magnetic field with phase speed given by, $(\frac{\mathbf{B_0}^2}{\mu\rho_0})^{\frac{1}{2}}$, called the Alvén speed.

3

Data Aquisition and Instrumentation

In this chapter I first describe the method in which the images are taken and processed to be sued for scientific purposes. In the next section the instrument (AIA/SDO) used to make observations of these magnetic field structures are discussed.

Taking Observations

The first evidence for the existence of the corona was through observations during solar eclipses. The occultation of the solar disk by the moon revealed a visible outer atmosphere structured into streamers and plumes and extending far from the solar surface (Figure 3.1). This is known as the white-light corona and is due to scattering of photospheric light by coronal particles. Before the early 20th century the only way to view the corona was for a short period during a solar eclipse when the moon provides the necessary obscuration of the disk.

Figure 3.1: The white-light corona during a solar eclipse observed from the Marshal Islands on 22 July 2009. Occultation of the bright solar disk by the moon reveals the faint outer atmosphere of the Sun, known as the corona. It is highly structured, showing features such as streamers and plumes. *Eclipse photograph courtesy of Miloslav Druckmüller http://www.zam.fme.vutbr.cz*

Image Data Reduction

All CCD images, have a number of basic image processing steps in common. The levels are the indicative of the corrections that has been done to the most basic of the levels, with the most basic raw data product of the telescope being level-0. Level-0 usually comprises the compressed raw data that comes directly from the spacecraft telemetry stream via the DPS. The data is processed from level-0 to level-0.5 by decompressing the spacecraft data and re-packaged into Flexible Image Transport System (FITS) files, which is an open standard format for all astronomical images. Calibration of the data into a scientifically usable format results in level-1 data. The steps to produce level-1 data are as follows:

- *Bias image subtraction.* The CCD of a camera will carry some charge in its pixels due to noise in the camera electronics. These are usually exposed by taking an image with the shutter closed and for the shortest possible exposure times. The bias image is subtracted from the raw image.

- *Dark current image subtraction.* Each CCD will carry some level of residual charge even when the camera shutter is closed. This residual charge is due to thermal energy of the CCD electrons and builds up over a finite exposure time. The voltage (thermal energy) must be removed from the raw image since it is not due to light from an observed source. The 'dark image' is taken with the camera shutter closed and an exposure performed as normal (exposure time the same as the raw image). The dark image is simply subtracted from the raw image. Note also that dark images will also contain a bias, so darks must be bias-subtracted before they are used on the raw image.

- *Flat-field correction.* Every CCD will have a non-uniform response across its photon collecting area. One side of the CCD, or any arbitrary grouping of pixels, may naturally be more sensitive than the other pixels. As well as this, the optical system itself may produce some brightness variation across the focal plane. To account for this, the raw image must be divided by a 'flat-field' in order to normalize the spatially non-uniform response detected by the CCD. The 'flat-field' is an image taken of a uniformly illuminated surface. For space-based telescopes this uniformly illuminated image is usually taken by closing the telescope front aperture and lighting a lamp placed near the aperture cover, or the telescope front door may contain a 'diffuser' that scatters sun light to provide uniform illumination. It is important that the dark and bias images be subtracted from the flat-field before the raw images (which are also dark and bias image subtracted) is divided by the flat field.

Accounting for dark current, bias, and flat-fielding are the most fundamental of all CCD imaging calibration routines. They can be summarised as

$$I_{cal}(x_i, y_i) = \frac{I_{raw}(x_i, y_i) - I_{dark-b}(x_i, y_i) - I_{bias}(x_i, y_i)}{|I_{flat}(x_i, y_i) - I_{dark-b}(x_i, y_i) - I_{bias}(x_i, y_i)|} \tag{3.1}$$

where I are the images, (x_i, y_i) are pixel coordinates, and the $|\ |$ in the denominator mean that the dark and bias-subtracted flat-field is normalized (divided by itself). I_{dark-b} is a de-biased dark image. Other standard techniques beyond the most basic ones include

- *Vignetting.* All camera imaging systems suffer from vignetting, a reduction in brightness at the edge of the field of view. In coronagraph systems this is particularly important since a vignette can occur at the inner field of view, due to the occulting disk and also due to the pylon supports of the disk. Special vignetting calibration images are performed to account for this effect; they are used to normalise the image in the same way as the flat-field is performed.

- *De-warping.* The image may suffer some geometric distortions due to a deformity in any one of the numerous optical components of the telescope.

This may result in the image being warped. Pre-flight experiments completely characterize any optical distortion so that all raw images may be 'de-warped'.

- *Brightness calibration.* This is the conversion from CCD data numbers per second ($\mathrm{DN\,s^{-1}}$) to physical measures of intensity e.g., mean solar brightness (MSB) units (1 MSB = $2.01 \times 10^{10}\,\mathrm{ergs\,s^{-1}\,cm^{-2}\ sr^{-1}}$). The conversion factors may be calculated in a pre-flight lab, or during inflight observations of objects with known intensities.

The above steps are the most frequently taken to ensure clean and calibrated astronomical images. They apply to every telescope using a CCD imaging system and every telescope type, including ground and spaced-based systems. Anything beyond the above calibration steps is termed level-2 and is usually instrument specific or specific to the scientific goal. In certain instances the image may be contaminated by cosmic ray detections on the CCD. Cosmic ray removal techniques are also specific to the observation, depending on the level of contamination. The removal techniques range from a simple manual masking of the contaminated areas of the CCD, to more sophisticated smoothing algorithms or multi-scale cleaning. The observations presented in this thesis were not badly contaminated by cosmic ray detections, so were their removal was not of concern in this instance.

Observations Instrument

Ultraviolet imaging can provide observations of the high temperature, low corona corona. Quiet coronal plasma temperatures of $\sim 1 \times 10^{6}\,\mathrm{K}$, up to flaring temperatures on the order of $\sim 10^7$ K, can produce a variety of ionization species of heavy elements such as Fe, O, Mg, or Si, for example. These ionization species are strong emitters in the ultraviolet and extreme ultraviolet wavelengths. Any imagers that have bandpasses centered on such wavelengths can therefore allow us to observe a variety of quiet and active coronal processes such as flares and large scale coronal bright fronts. All ultraviolet imagers of the corona are space-based, the latest of this fleet of telescopes is the Atmospheric Imaging Assembly (AIA) on board the *Solar Dynamics Observatory* (*SDO*; Lemen et al., 2012a), launched in 2010.

The Atmospheric Imaging Assembly

SDO is in a geosynchronous orbit at 102° W longitude, inclined at 28.5°. The on-board ultraviolet imager, AIA, consists of four Cassegrain telescopes (Figure 3.2) that provide visible, ultraviolet (UV), and extreme ultraviolet (EUV) full-disk images of the transition region and corona up to $0.5\,R_\odot$ above the photosphere with $0.6''$ spatial resolution and 12-second temporal resolution (Lemen et al., 2012a). The telescopes provide imaging in seven extreme ultraviolet passbands centered on the lines of Fe XVIII (94 Å), Fe VIII, XXI (131 Å), Fe IX (171 Å), Fe XII, XXIV (193 Å), Fe XIV (211 Å), He II (304 Å), Fe XVI (335 Å). One of the telescopes observes longer wavelengths at C IV (1600 Å), the nearby continuum at (1700 Å) and a broadband visible filter centered on (4500 Å) giving a full temperature coverage of 5×10^3 K to 2×10^7 K.

Each telescope has a field of view of $41'$ circular diameter, a 20 cm primary mirror and an active secondary mirror that is pointed in response to signals from

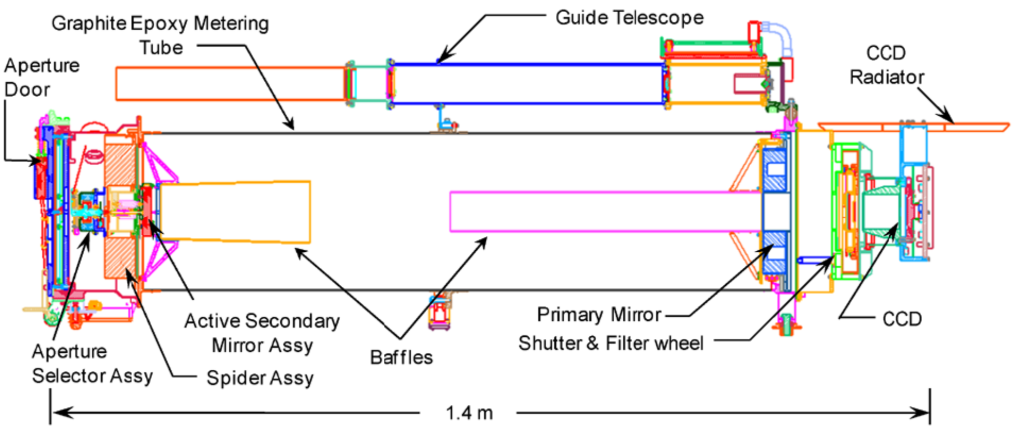

Figure 3.2: The Atmospheric Imaging Assemly (AIA) telescope design. AIA employs four Cassegrain type telescopes, with telescope 1, 2 and 4 serving as dual channel passbands, and telescope 3 permitting imaging at three separate passbands (Lemen et al., 2012a).

a guide telescope. Each mirror is polished to a roughness of < 5 Å rms in the spatial frequency range 10^{-3}–5×10^{-1} nm^{-1}. The primary mirror in each telescope has a different multi-layer coating on either half, making it reflective to two wavelengths. For example, half of mirror 2 has a peak reflectance at 195.5 Å with the other half reflects at 211.3 Å. Half of mirror 3 provides the broadband UV and visible channel, with a coating that gives the ability to reflect at 1600, 1700, and 4500 Å, while the other half of the mirror provides the primary optics for the 171 Å channel. Hence telescope 3 provides the optics for four different bandpasses. The coronal plasma temperature response of each telescope channel is shown in Figure 3.3.

Metal entrance filters at the aperture of each telescope, combined with a filter wheel located in front of each focal plane, suppress unwanted UV, visible, and infrared radiation. The filters are either made of aluminium, used for wavelengths of 171 Å or longer, and zirconium used for the shorter 94 Å and

131 Å wavelengths. Telescope 3 has an aluminium (for 171 Å) and MgF–2 (for the UV broadband) entrance window and 3 different filters on the filter wheel that cater for observation in 171 Å (aluminium), 1600 Å (MgF−2), 1700 Å and 4500 Å (fused silica). A mechanical shutter regulates exposure time to a nominal short exposure of 5 ms and nominal long exposure of 80 ms. Flight software can also select any custom exposure time. The focal plane of each telescope contains a back-illuminated 4096×4096 pixel CCD, with each square pixel having a 12 μm size. Each CCD is read out in 4 quadrants, via an amplifier, into a camera box with four interfaces (one for each quadrant). Each quadrant is read out at a rate of 2 Mpixels s^{-1} and data transmission to the on-board computer occurs at a rate of 100 Mb s^{-1} All of the steps above described for white-light calibration are relevant for ultraviolet CCD imaging also. The AIA calibration procedure to bring the data from level-0.5 to level-1 include de-biasing, dark subtraction, flat-fielding, de-vignetting, de-warping, and brightness calibration, as described in the white-light calibration section. Some example images of AIA are shown in Figure 1.8.

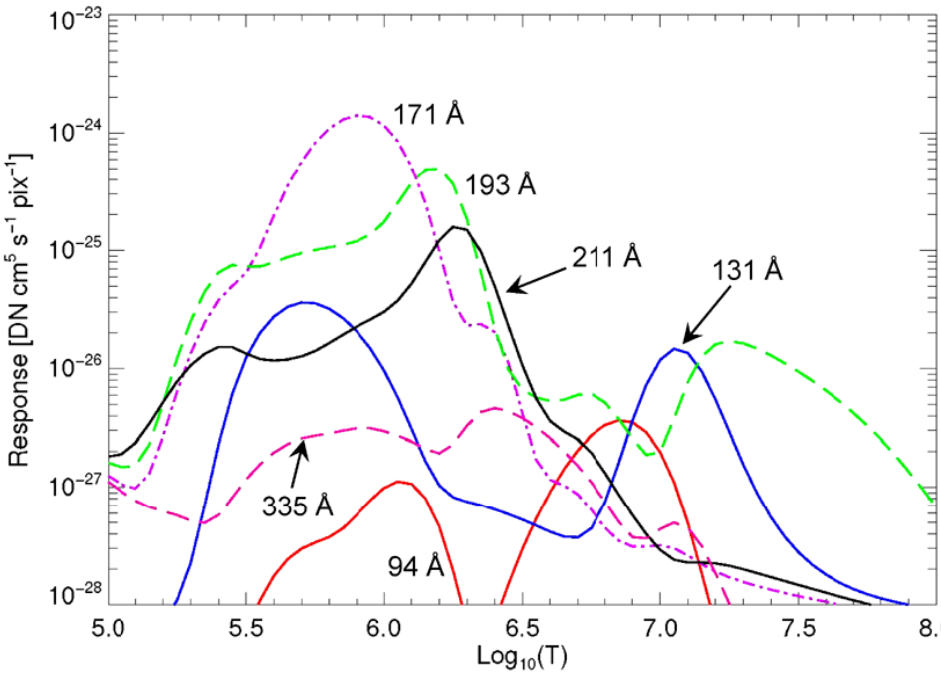

Figure 3.3: The Atmospheric Imaging Assembly temperature responses for each of its passbands. The passbands cover temperatures that include the transition region, to quiet corona, to flaring corona. The 4500 Å passband is not shown here, its temperature coverage results in photospheric imaging (Lemen et al., 2012a).

4
Waves in Plume

Introduction

Plumes are defined as the plasma density enhancements along the magnetic field lines, in the corona (Wilhelm et al., 2011). They are one of the prominent features in the solar corona visible both in visible and UV radiations. The association between the polar plumes and the magnetic flux concentrations was first pointed out by (Saito, 1958). Plumes are found to be originating from the supergranular network boundaries, as indicated by (DeForest et al., 2001). Plumes are almost five times denser than the interplume regions at the base of the corona (Wilhelm et al., 2011). The footpoints of the plume are about $4''$ and plumes are observed to expand with height(Deforest et al., 1997).

Compressional waves in polar plumes were first proposed by (Ofman et al., 1997). Quasi periodic intensity variations in plumes was reported using data from EIT (DeForest & Gurman, 1998). Periodicities of intensity variation along plumes ranged from 10-15 minutes. Oscillations in hot loops were first discovered by

SUMER/*Solar and Heliospheric Observatory (SOHO)*, as periodic variations of doppler shift, which were interpreted as standing slow mode waves (Wang, 2011; Wang et al., 2003). The origin of these waves was traced to the flare at one of the loop footpoints (Wang et al., 2005). An impulsive onset of flow or a velocity pulse at one of the loop footpoints leads to the generation of standing slow wave modes(Ofman & Selwa, 2009; Ofman et al., 2012). These oscillation decay rapidally, simulations (Selwa et al., 2005) suggested that the pressure pulses generated close to a footpoint cannot excite a fundamental slow mode fast enough to compensate for the strong damping. It is also shown (Ofman & Wang, 2002) that thermal coduction is one of the major damping mechanism of such standing slow waves in hot coronal loops. An extensive study of such standing waves in coronal loops is presented by (Wang et al., 2015).

In this study we report first SDO/AIA observation which shows clear signatures of a standing slow wave, in an cool open magnetic field structure. We also find signature of reflection from the plume.

Observation and Data Analysis

A GOES X1.0-class flare occured on 2014 March 29 at 17:35 UT from NOAA active region AR 12017, located at $462''$ & $297''$. The shock generated, reached the plume located at $223''$ & $701''$. Soon after that we noted the intensity oscillations in the plume. To analyse these intensity variation we obtained the data from both the 193 Å and 171 Å channels from 17:20 UT to 18:30 UT on 2014 March 29, from JSOC. The data used for this study was obtained from AIA (Lemen et al., 2012b) on board SDO. AIA/SDO provides full-disk solar images in seven

EUV and three UV-visible channels covering a temperature range from 6×10^4 K to 2×10^7 K. The instrument records images of the sun with a spatial resolution of $1.5''$ and temporal resolution of 12s. The downloaded *level 1.0* data is then reduced to *level 1.5* using the *aia_prep.pro*, making the necessary instrumental corrections such as performing image registration (rotation, translation, scaling) and updating the header information. The AIA images have a pixel size of $0.6''$ in both X and Y directions. The *level 1.5* data was derotated to correct for the

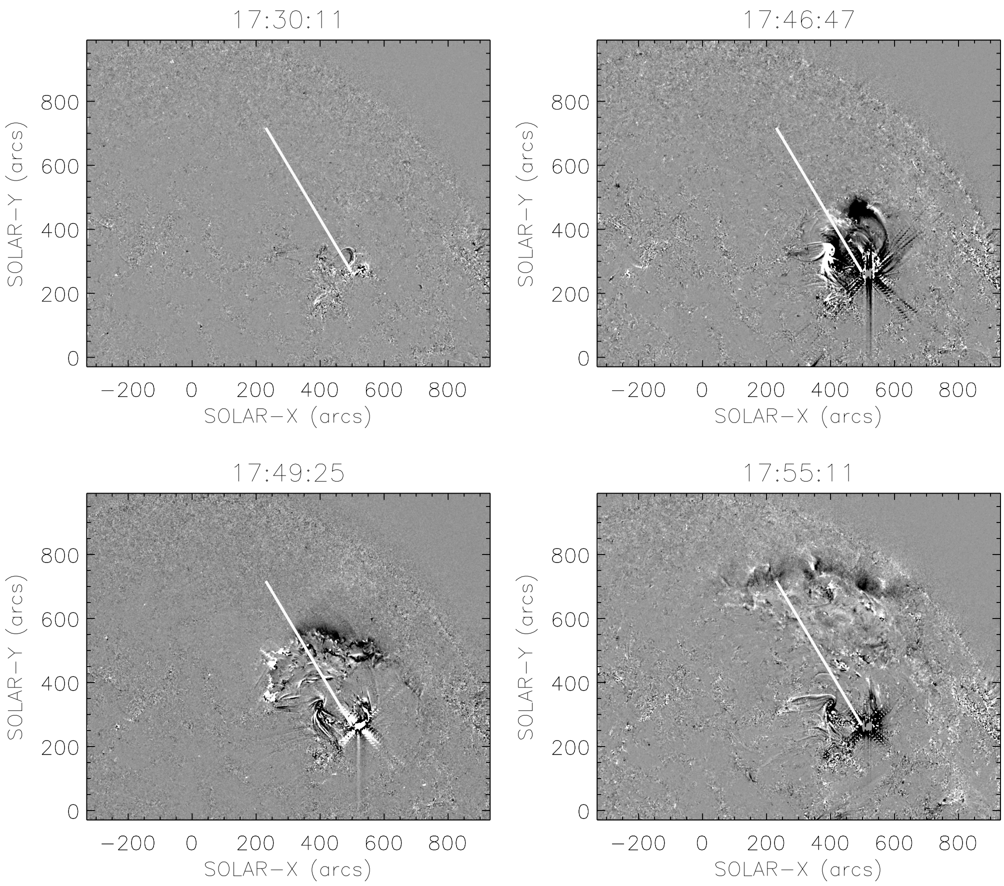

Figure 4.1: Running difference image sequence at four different times, in 171 Å. Shock front propagating outwards is clearly seen. Artificial slit, represented by white line was placed perpendicular to the shock front.

differential rotation of the sun. The data was then smoothened to increase the signal-to-noise ratio. Multiwavelength data from AIA 171 Å and 193 Å was used for this analysis. In case of 171 Å there were some missing frames. These missing frames were replaced by synthetic pixel-by-pixel interpolated frames to make the dataset uniform. When there was a flare the exposure time was reduced in 193 Å from insert value from to the vale to as a result the signal-to-noise ratio is very poor at those times in 193 Å. To build up signal-to-noise ratio in these case the frames are replaced with median filtered image of five frames before and after the bad frame. We also made the running-difference images to illustrate the dynamic features clearly. A time-lapse movie was created from the final images obtained after doing the aforementioned processing. We also noticed that the visibility of the plume is better in 171 Å than 193 Å. In case of 193 Å the plume is visible along with several other hot loops thus contaminating the original structure of the plume. Figure 4.1 shows the running difference image in the 171 Å at four different time instances of 17:30 UT, 17:46 UT, 17:49 UT and 17:55 UT. The difference images as shown in Figure 4.1 show the shock propagating outwards from the NOAA active region AR12017 situated at the base of the artificial slit shown in white in Figure 4.1.

An artificial slit was placed perpendicular to the shock front shown in Figure 4.1, to estimate the speed of the shock. The time-distance map (henceforth referred to as x-t map), Figure 4.2 was generated corresponding to the artificial slit in Figure 4.1. A straight line was fitted on the inclined ridge on the x-t map in Figure 4.2 to find its slope. To fit a line the end positions on the ridge were chosen manually and a gaussian curve was fitted, in the neighborhood about each point on the slit. The maxima of the fitted gaussian was used to fit a straight

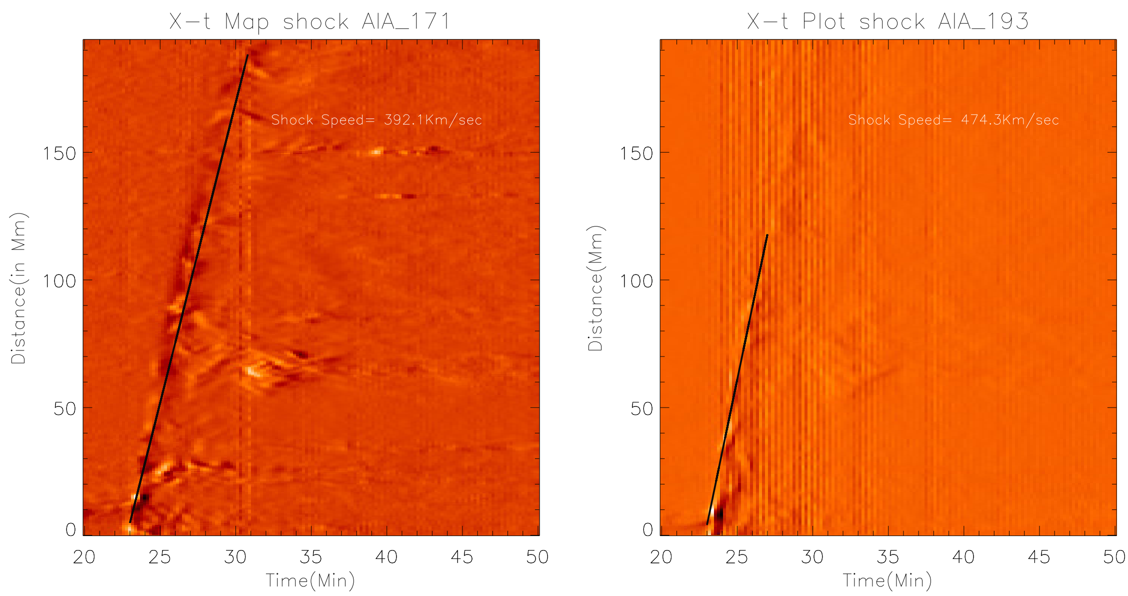

Figure 4.2: Time distance map, corresponding to the slit position marked in white as shown in Figure 4.1 to estimate the shock speed. The estimated speeds are shown in the panels.

line. The slope of this line was estimated using least-square-fitting. The slope of the fitted line is shown in the x-t map Figure 4.2. We estimated the speed with which the shock hits the plume to be $\sim 392 \pm 6.2$ Kms^{-1} in 171 Å and $\sim 474 \pm 8.3$ Kms^{-1} in 193 Å.

The movies generated from the processed images showed intensity oscillations in the plume. The movies in 193 Å also showed diffused plume because of the presence of hot loops seen in 193 Å. To further understand the nature of these oscillations artificial slits were placed in the plume. The plume also had an oscillation in the spatial direction to make sure that we capture most of the oscillations, a wide slit (8 pixels) was chosen. The slit location for 171 Å and 193 Å is shown in Figure 4.3 top panels left corresponding to 171 Å and right corresponding to 193 Å.

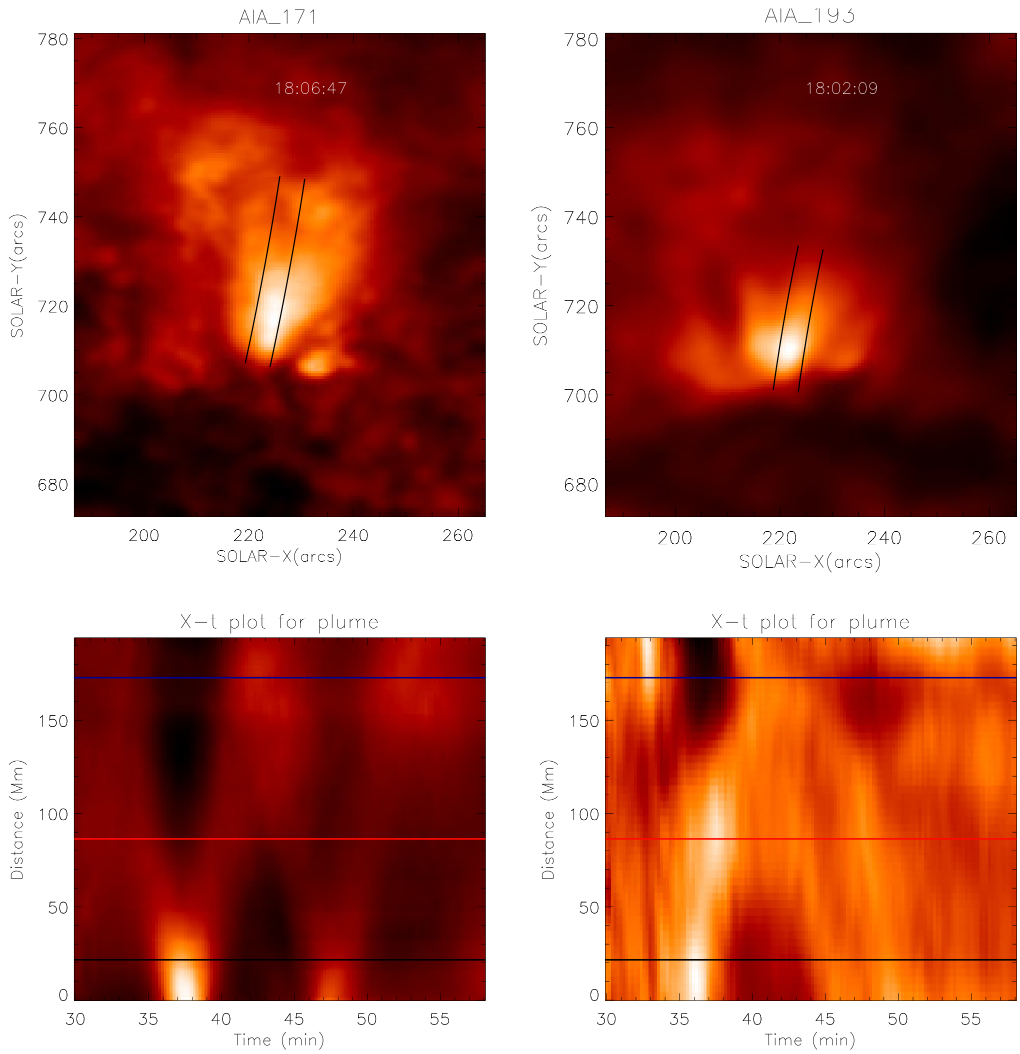

Figure 4.3: Artificial slits, placed on the plume in the top panel, having width 8 pixels, to analyse the intensity oscillation in plume. Time distance maps obtained for the corresponding slits are shown in the lower panels.

The slits for 171 Å and 193 Å is not coaligned as the 193 Å is also responsive for the hotter coronal loops, making the plume appear diffused. The x-t maps corresponding to the slits selected in Figure 4.3 for both 171 Å and 193 Å are shown in lower panel of Figure 4.3. As the shock hits the plume it compresses the plasma inside and then this plasma undegoes rarefaction. The alternate light and dark patches in the x-t maps of Figure 4.3 shows compression and rarefaction, respectively of the enclosed plasma, which is a signature of compressional wave.

To furter study the variation of intensity we plotted the relative intensity at the different locations of the plume for 171 Å marked in Figure 4.3, with blue, red and black lines corresponding to top, intermediate and base of the plume respectively, along the height of the plume, shown in Figure 4.4. The correlation coefficient between the intensity variation at the base and top of the plume is calculated to be -0.92 for 171 Å and -0.91 for 193 Å respectively. The correlation analysis suggested that these are anti-correlated. Similar analysis was performed using 193 Å. The intensity variation along the base and top of the plume differ by a phase difference of 180° and also it is almost zero near the intermediate position of the plume. From the analysis of the x-t map of the plume as shown in Figure 4.3 and further from the time evolution of intensity variation along the height of the plume as shown in Figure 4.4, we conclude that the oscillations that we find are indeed standing oscillations.
Also from plots of intensity variation Figure 4.4 we see that the oscillation changes phase and decreases in amplitude as we go from the base of the plume to the top of the plume, thus confirming the presence of the standing waves in the plume. A damped sinusoidal function

$$y = A_0 \exp\left(-\lambda t\right) \sin\left(\frac{2\pi t}{A_1} + A_2\right) + A_3 \tag{4.1}$$

where, $A_0$is the amplitude of the wave and A_1 is the inverse of time period and λ gives the damping time, was fitted to get the parameters of the wave and the period was found to be roughly 11 mins.

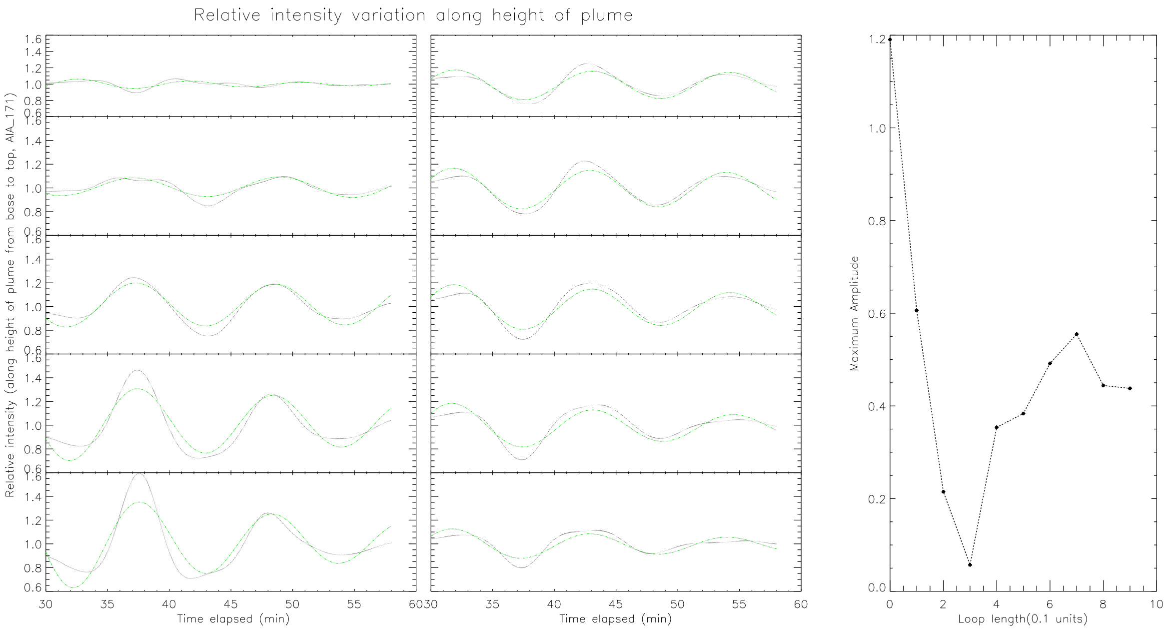

Figure 4.4: Intensity variations along the height of the plume. The right panel shows the intensity variations at different height of the plume from base to top. Dotted line is the original curve and green line is the fitted curve. The extreme right panel shows the change in maximum amplitude along the height of plume.

DEM analysis

Wave propagation through a medium depends on the physical parameters of the medium, such as density, temperature etc. To understand the nature of the surrounding of the plume under consideration we performed the Differential-Emission-Measure (DEM) analysis of the plume as suggested by (Aschwanden et al., 2013). The temperature distribution of the corona can quantitatively be expressed by the so-called differential emission measure distribution (DEM). The DEM indicates theamount of plasma along the line of sight that is emitting radiation originating at temperatures between T and T+dT. Images from six

!

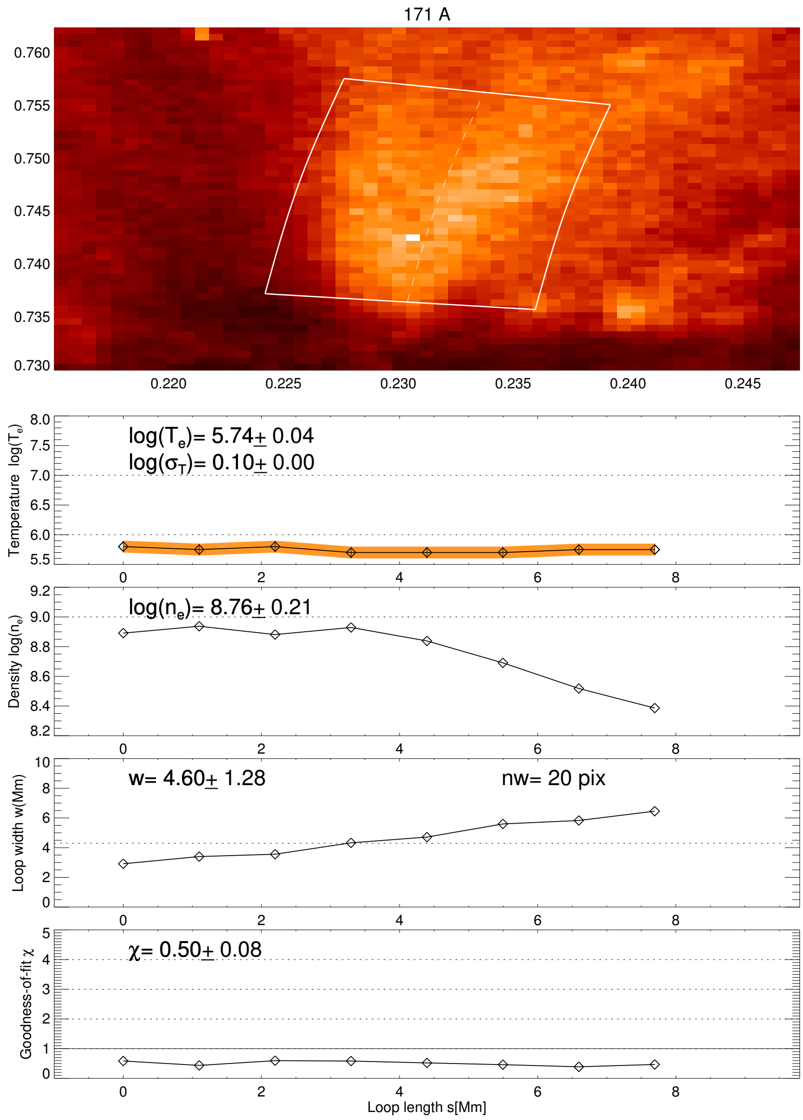

Figure 4.5: Automated DEM analysis,top panel shows loop as seen in 171 Å. The estimated width, loop density (n_e), loop temperature (T_e) and goodness of fit (χ) is also plotted in the bottom panels.

different coronal filters were obtained before the shock reached the plume. The first step in doing DEM analysis is coalignmnet of the images in six EUV coronal filters, namely 94 Å, 131 Å, 171 Å, 193 Å, 211 Å, 335 Å, the chromospheric heights are calculates using solar limb fit. The loop temperature is found to be constant ≈ 0.1MK using DEM analysis. Along the height of the plume from the base to the top the density (n_e) decreases Figure 4.5 third panel from top. The density decreased along the height following the function

$$y = a_0 + a_1 x^2 + a_2 x \tag{4.2}$$

where, a_0= 8.88, a_1 = 0.05 a_2 = -0.015 .

Conclusions

In this study we report, for the first time the standing mode oscilations supported by cool and open magnetic field structure, such as plume. These waves were triggered by the incoming shock from the GOES X1.0 class flare. As reported by (Wang et al., 2003, 2005; Yuan et al., 2015) the standing slow waves is produced by a flare at one of the footpoints of the loop, we further add that the shock coming from a distance as well can trigger such standing waves in a loop. The speed of the wave is 108 km/sec and this is comparable to the speed of the sound in 171 $\mathring{A}$ DEM analysis performed on the AIA image sequence before the shock from the flare reaches the plume gives us a temperature ≈ 0.1MK and a gradient in density which is dependent on height shown in Eq. 4.2, which decreases from the base of the plume to the top of the plume. The density profile calulated gives an initial condition for the modelling of standing waves in open magnetic field structures. The situation here is identical to the reflection from an open pipe with nodes at the base and the top of the plume and the internode is at the midposition. From our analysis we report first observational evidence of standing oscillations supported by open field magnetic structures, in this case the plumes. We also provide a density profile for the modelling of such standing waves in open magnetic field structures.

5

Conclusions

The first goal of this research was to study the Sun, the energy generation mechanism and also the way it produces and sustains the magnetic field. One of the holy grail of solar physics is the Coronal Heating Problem, now there is strong concensus that the waves in the atmosphere might be able to explain this problem. Waves in different magnetic field structures found in corona. The plumes as they are thought to be liked with the solar wind are defenitely interesting. In the present study we report that the open magnetic field structures are also able to

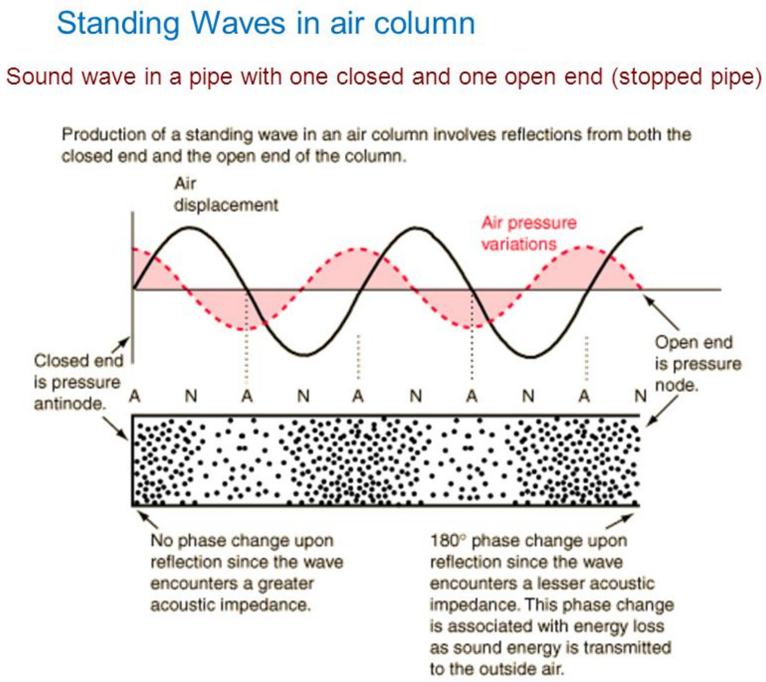

Figure 5.1: The reflection from an open pipe, the nodes are at the closed end and at teh boundaryof the pipe and the outside.

support standing magnetoacoustic waves. In this chapter, I will summarise and conclude this research and outline the future of this study.

Plume Oscillations: Principle Results

We find signature of standing waves in open magnetic field structure, plume. The situation here is the somewhat as that of the reflection from a open pipe as shown in Figure 5.1. The nodes being at on of the anchored position and the other at a boundary of the interface. We also notice these to be damped. The frequency of these waves was found to be, 10.97 secs and velocity was 108 km/sec. The density along the height of the plume was found to be decreasing, providing with a model for the density profile that is needed to sustain such standing waves in open magnetic field structutres.

Furure Work

The next step is to to simulate this finding and derive the constraints for sustaining such a phenomenon.

References

Aschwanden, M. J. 2004, Physics of the Solar Corona. An Introduction (Praxis Publishing Ltd) (Cited on pages 10 and 16.)

Aschwanden, M. J., Boerner, P., Schrijver, C. J., & Malanushenko, A. 2013, *Solar Physics*, 283, 5 (Cited on page 52.)

Babcock, H. W. 1961, *Astrophysical Journal*, 133, 572 (Cited on page 11.)

Bouvier, A., & Wadhwa, M. 2010, Nature Geoscience, 3, 637 (Cited on page 2.)

Carlsson, M., & Stein, R. F. 1997, *Astrophysical Journal*, 481, 500 (Cited on page 18.)

Charbonneau, P. 2010, Living Reviews in Solar Physics, 7, 3 (Cited on page 10.)

Davis, R., Harmer, D. S., & Hoffman, K. C. 1968, Physical Review Letters, 20, 1205 (Cited on page 4.)

De Pontieu, B., Erdélyi, R., & James, S. P. 2004, *Nature*, 430, 536 (Cited on page 19.)

DeForest, C. E., & Gurman, J. B. 1998, *Astrophysical Journal Letters*, 501, L217 (Cited on page 45.)

Deforest, C. E., Hoeksema, J. T., Gurman, J. B., et al. 1997, *Solar Physics*, 175, 393 (Cited on page 45.)

REFERENCES

DeForest, C. E., Lamy, P. L., & Llebaria, A. 2001, *Astrophysical Journal*, 560, 490 (Cited on page 45.)

Fan, Y. 2009, Living Reviews in Solar Physics, 6, 4 (Cited on page 12.)

Fontenla, J., Reichmann, E. J., & Tandberg-Hanssen, E. 1988, *Astrophysical Journal*, 329, 464 (Cited on pages 15, 16, 17 and 21.)

Foukal, P. V. 2004, Solar Astrophysics, 2nd, Revised Edition (Wiley-VCH) (Cited on pages 2 and 5.)

Gabriel, A. H. 1976, Royal Society of London Philosophical Transactions Series A, 281, 339 (Cited on pages 15, 16, 17 and 21.)

Lemen, J. R., Title, A. M., Akin, D. J., et al. 2012a, *Solar Physics*, 275, 17 (Cited on pages 40, 41 and 43.)

—. 2012b, *Solar Physics*, 275, 17 (Cited on page 46.)

McAteer, R. T. J., Gallagher, P. T., Williams, D. R., et al. 2002, *Astrophysical Journal Letters*, 567, L165 (Cited on page 18.)

Mitalas, R., & Sills, K. R. 1992, *Astrophysical Journal*, 401, 759 (Cited on page 5.)

Montmerle, T., Augereau, J.-C., Chaussidon, M., et al. 2006, Earth Moon and Planets, 98, 39 (Cited on page 2.)

Ofman, L., Romoli, M., Poletto, G., Noci, G., & Kohl, J. L. 1997, *Astrophysical Journal Letters*, 491, L111 (Cited on page 45.)

Ofman, L., & Selwa, M. 2009, in IAU Symposium, Vol. 257, Universal Heliophysical Processes, ed. N. Gopalswamy & D. F. Webb, 151–154 (Cited on page 46.)

Ofman, L., & Wang, T. 2002, The Astrophysical Journal Letters, 580, L85 (Cited on page 46.)

Ofman, L., Wang, T. J., & Davila, J. M. 2012, *Astrophysical Journal*, 754, 111 (Cited on page 46.)

Sackmann, I.-J., Boothroyd, A. I., & Kraemer, K. E. 1993, *Astrophysical Journal*, 418, 457 (Cited on pages 2 and 3.)

Saito, K. 1958, *Publications of the Astronomical Society of Japan*, 10, 49 (Cited on pages 23 and 45.)

Schrijver, C. J., & Zwaan, C. 2008, Solar and Stellar Magnetic Activity (Cited on page 15.)

Selwa, M., Murawski, K., & Solanki, S. K. 2005, *Astronomy & Astrophysics*, 436, 701 (Cited on page 46.)

Thompson, M. J., Christensen-Dalsgaard, J., Miesch, M. S., & Toomre, J. 2003, *Annual Review of Astronomy & Astrophysics*, 41, 599 (Cited on page 8.)

Turck-Chièze, S., & Couvidat, S. 2011, Reports on Progress in Physics, 74, 086901 (Cited on pages 4 and 6.)

Vernazza, J. E., Avrett, E. H., & Loeser, R. 1981, *Astrophysical Journal Supplemental Series*, 45, 635 (Cited on pages 15, 16, 17 and 21.)

Wang, T. 2011, *Space Science Reviews*, 158, 397 (Cited on page 46.)

Wang, T., Ofman, L., Sun, X., Provornikova, E., & Davila, J. M. 2015, *Astrophysical Journal Letters*, 811, L13 (Cited on page 46.)

Wang, T. J., Solanki, S. K., Curdt, W., et al. 2003, *Astronomy & Astrophysics*, 406, 1105 (Cited on pages 46 and 54.)

Wang, T. J., Solanki, S. K., Innes, D. E., & Curdt, W. 2005, *Astronomy & Astrophysics*, 435, 753 (Cited on pages 46 and 54.)

Wilhelm, K., Abbo, L., Auchère, F., et al. 2011, *Astronomy & Astrophysics Review*, 19, arXiv:1103.4481 (Cited on page 45.)

Yuan, D., Doorsselaere, T. V., Banerjee, D., & Antolin, P. 2015, The Astrophysical Journal, 807, 98 (Cited on page 54.)